












# Targeting lymphoid-derived IL-17 signaling to delay skin aging

Received: 23 December 2021

Accepted: 2 May 2023

Published online: 8 June 2023

 Check for updates

Paloma Solá <sup>1,5</sup>, Elisabetta Mereu <sup>2,5</sup>, Júlia Bonjoch<sup>1,6</sup>,  
Marta Casado-Peláez <sup>2,6</sup>, Neus Prats<sup>1</sup>, Mònica Aguilera <sup>1</sup>, Oscar Reina<sup>1</sup>,  
Enrique Blanco <sup>3</sup>, Manel Esteller<sup>2,4</sup>, Luciano Di Croce<sup>3,4</sup>, Holger Heyn <sup>3</sup> ,  
Guiomar Solanas <sup>1</sup>  & Salvador Aznar Benitah <sup>1,4</sup> 

Skin aging is characterized by structural and functional changes that contribute to age-associated frailty. This probably depends on synergy between alterations in the local niche and stem cell-intrinsic changes, underscored by proinflammatory microenvironments that drive pleiotropic changes. The nature of these age-associated inflammatory cues, or how they affect tissue aging, is unknown. Based on single-cell RNA sequencing of the dermal compartment of mouse skin, we show a skew towards an IL-17-expressing phenotype of T helper cells,  $\gamma\delta$  T cells and innate lymphoid cells in aged skin. Importantly, *in vivo* blockade of IL-17 signaling during aging reduces the proinflammatory state of the skin, delaying the appearance of age-related traits. Mechanistically, aberrant IL-17 signals through NF- $\kappa$ B in epidermal cells to impair homeostatic functions while promoting an inflammatory state. Our results indicate that aged skin shows signs of chronic inflammation and that increased IL-17 signaling could be targeted to prevent age-associated skin ailments.

Aging is caused by cellular damage accumulation due to ineffective metabolism, circadian clock rewiring and increased systemic inflammation, leading to dysfunction and eventual organismal collapse when challenged<sup>1–6</sup>.

The skin contains a multilayered epidermis interspersed with hair follicles and sebaceous glands. The outermost layer of the skin, the epidermis, is a stratified epithelium that forms an impermeable protection for the organism. Daily renewal of the epidermis is fueled by interfollicular epidermal stem cells whereas hair follicle stem cells maintain hair follicles by periodical generation of new hair shafts<sup>7</sup>. In the dermis, an organized mesh of extracellular matrix (ECM) embedded with distinct cell types forms the niche for all epidermal stem cells<sup>7</sup>. Epidermal aging is characterized by alterations in its regenerative potential and barrier functions<sup>8–12</sup>. Moreover, age-related changes in the dermal cellular composition and ECM properties affect its functionality, both as a structural scaffold and as a niche for epidermal

stem cells<sup>13–18</sup>. Collectively these changes lead to a slower epidermal turnover, breaching of the barrier and lower quality of wound healing, all of which contribute to increasing the incidence of infections and chronic traits in the elderly<sup>19–21</sup>.

Previous single-cell RNA sequencing (scRNA-seq) studies focused on defining changes in skin cell types during homeostasis, aging and disease suggest that some immune cell types change their abundance or behavior during aging in skin<sup>13,22–29</sup>. However, much remains unknown regarding the relationship between immune cells of the dermis and other dermal and epidermal cells during aging.

Here we unbiasedly profiled and characterized the single-cell transcriptome of dermal cells in aged skin in mice. CD4<sup>+</sup> T helper (T<sub>H</sub>) cells,  $\gamma\delta$  T cells and innate lymphoid cells (ILCs) showed the most prominent changes during aging and appeared to orchestrate many of the alterations observed in the aged skin. Specifically, these cells became polarized towards an IL-17-producing phenotype, strongly contributing

<sup>1</sup>Institute for Research in Biomedicine, Barcelona Institute of Science and Technology, Barcelona, Spain. <sup>2</sup>Josep Carreras Leukemia Research Institute, Badalona, Spain. <sup>3</sup>Centre for Genomic Regulation, Barcelona Institute of Science and Technology, Barcelona, Spain. <sup>4</sup>ICREA, Catalan Institution for Research and Advanced Studies, Barcelona, Spain. <sup>5</sup>These authors contributed equally: Paloma Solá, Elisabetta Mereu. <sup>6</sup>These authors contributed equally: Júlia Bonjoch, Marta Casado-Pelaez. ✉e-mail: [holger.heyn@cnag.org.eu](mailto:holger.heyn@cnag.org.eu); [guiomar.solanass@irbbarcelona.org](mailto:guiomar.solanass@irbbarcelona.org); [salvador.aznar-benitah@irbbarcelona.org](mailto:salvador.aznar-benitah@irbbarcelona.org)

to the inflammatory environment found in aged skin. Importantly, in vivo blockade of IL-17 signaling during the aging process delayed the development of several hallmarks of skin aging, resembling the state of adult skin.

## Results

### Aged dermal cells reveal cell type- and age-specific changes

We analyzed the nonepithelial (negative for epithelial cell adhesion molecule (EpCAM<sup>-</sup>)) dermal population of dorsal skin from aged (80- to 90-week-old) and adult (17- to 25-week-old) mice by scRNA-seq. We removed epidermal cells enzymatically and isolated dermal cells by fluorescence-activated cell sorting (FACS) (Fig. 1a and Extended Data Fig. 1a). To maximize sampling of less abundant immune cells, we enriched by FACS for CD45<sup>+</sup> cells and sequenced these separately from other dermal cells (EpCAM<sup>-</sup>CD45<sup>-</sup>) (Extended Data Fig. 1a). Using the 10X Genomics platform (v.3) we characterized 11,940 cells for CD45<sup>+</sup> cells and 5,213 for their CD45<sup>-</sup>EpCAM<sup>-</sup> counterparts. After batch correction and data integration, we verified good sample mixing<sup>30</sup> and representation of all replicates across all populations (Extended Data Fig. 1b,c). We clustered all cells by generation of a shared nearest-neighbor graph using the Louvain algorithm<sup>31</sup> and visualized clustering with uniform manifold approximation and projection (UMAP). We then performed differential gene expression between cell populations to obtain cluster markers (Fig. 1b and Supplementary Table 1) and plotted discriminatory population markers to ensure correct clustering (Fig. 1c). In UMAP visualization we observed three major groups of clusters pertaining to nonimmune (CD45<sup>-</sup>EpCAM<sup>-</sup>), immune myeloid and immune lymphoid lineages (both CD45<sup>+</sup>) (Fig. 1b,c).

**Nonimmune cells.** Although we detected clusters for endothelial cells, along with pericytes and Schwann cells (Fig. 1b–d), fibroblasts were the most abundant CD45<sup>-</sup>EpCAM<sup>-</sup> cell type and were separated into five clusters containing subtypes with distinct features (Fig. 1d). Some of these clusters showed high similarity to well-defined fibroblast subtypes regarding marker expression—cluster 1 was reticular like, cluster 2 papillary like and cluster 3 proinflammatory<sup>23,24,32–34</sup>. Cluster fibroblast 1 included markers of dermal papilla cells<sup>35</sup>, a specialized cluster of fibroblasts located immediately beneath hair follicles that is essential for modulation of the hair follicle cycle (Fig. 1c,d).

With fibroblasts being the most predominant cell type in the dermis, their age-associated alterations probably affect neighboring cells. To further understand their age-related changes we analyzed the expression of senescence-related markers. The accumulation of senescent cells is suggested to be a key mechanism underlying aging<sup>3</sup>. These nonproliferating senescent cells generate a proinflammatory environment by secretion of an array of cytokines and ECM remodeling enzymes among others. Although detection of senescent cells in vivo is challenging, transcriptional upregulation of *Cdkn2a* (which encodes p16) and/or *Cdkn1a* (p21) is considered a sign of senescence<sup>3</sup>. We did not observe increased expression of these genes in our dermal nonimmune clusters, which include fibroblasts (Extended Data Fig. 2a and Supplementary Table 2). Besides, there was no upregulation of *Ifna* and *Ifnb1*, additional bona fide markers of senescence<sup>36</sup>. Moreover, there was no global difference in expression of the skin aging-associated secreted protein signature<sup>37</sup> in any of the fibroblast populations with aging (Extended Data Fig. 2b). This suggests that there is no increased expression of senescence in our dataset, which could have been caused by either a lack of sufficient depth to detect these marker changes in our experimental setup or to senescence not being a major driver of fibroblast aging in the age group analyzed.

The nonimmune compartment showed stable cell proportions during aging (Extended Data Fig. 2c). This was accompanied by transcriptomic changes in some populations, including fibroblasts 1 and 3 (Supplementary Table 2), which pointed towards an increase in their global proinflammatory state. Nevertheless, the changes observed by

10X scRNA-seq in these populations were subtle and did not allow for in-depth analysis of their specific age-related alterations.

**Immune cells.** Visual representation of immune cell clusters rendered two major cell groups, myeloid and lymphoid (Fig. 2a). We observed statistically significant changes in proportions in some immune populations during aging (Extended Data Fig. 3a,b).

To measure the effect of aging on the transcriptome of immune cells in a global and unbiased manner, we developed a deep learning model that quantifies the deviance of each immune cell type in aging. We assumed that the most age-affected cells would present the most altered transcriptomic changes compared with their adult counterparts and, therefore, would be more distant in multidimensional gene expression space. We used our 10X scRNA-seq data from adult mice as a reference to train our model for each different cell type signature and then evaluated the similarity between adult and aged cells within each cell type. Cells with the highest deviance in their identity were those accumulating more differences between ages. Notably, we found that CD4<sup>+</sup>T<sub>H</sub> cells,  $\gamma\delta$  T cells, ILCs and dendritic cells were the types with the highest age deviance, showing the highest proportion of cells affected by aging (Fig. 2b). This suggests that lymphoid cell subsets present the most predominant age-related changes. Focusing on lymphoid cells, UMAP representation of exclusively lymphoid cells showed that CD4<sup>+</sup>T<sub>H</sub> cells,  $\gamma\delta$  T cells and ILCs possess a large proportion of cells with a high age-deviance score (Fig. 2c).

Therefore, because cell proportion changes accompany transcriptomic changes in some dermal immune cells during aging, we focused our further analysis on these immune cell types.

### Aged dermal myeloid cells upregulate proinflammatory genes

Dermal myeloid cells balance pro- and anti-inflammatory functions in skin in a context-dependent manner<sup>38</sup>. Specifically, they scan the tissue to detect antigens, orchestrate an early response to pathogens and trigger the first steps in the wound-healing response<sup>39</sup>. We detected eight clusters of myeloid cells: macrophages 1–3, monocytes 1–3, dendritic cells and proliferating myeloid cells (Fig. 2a).

Monocyte 1 and macrophage 1 clusters were defined by proinflammatory features (for example, the former expressed *Ccr2*, *Cxcl2*, *Fcgr4* and *Cxcr4* and for macrophage 1 we obtained *Il1b*, *Tnfaip3* and MHC class II complex genes including *H2ab1*, *H2-Eb1*, *H2-Aa* and *Cd74*). Conversely, cluster macrophage 2 expressed regulatory macrophage markers including *Il4l1*, *Cd200r1* and *Lgals1* (Supplementary Table 1). Of note, although the proportion of both macrophage 1 and monocyte 3 clusters changed in aged tissue (Extended Data Fig. 3a) they showed no clear transcriptome variations (Supplementary Table 2). By contrast, monocyte 1 and 2 clusters showed more pronounced gene expression changes with aging, with a trend towards expression of higher levels of proinflammatory cytokine secretion and responses to proinflammatory stimuli (Extended Data Fig. 3c and Supplementary Tables 2 and 3). This included upregulation of the gene encoding IL-1 $\beta$  in monocyte 1 (Extended Data Fig. 3d), which is necessary for these cells to initiate a full immune response<sup>39</sup>. The expression of *Il1b* was also upregulated in clusters macrophage 2 and dendritic cells during aging (Extended Data Fig. 3d and Supplementary Table 2), indicating an increase in proinflammatory gene expression during aging.

Together, this indicates that myeloid cell activation exacerbates a chronic inflammatory state in aged skin.

### Increased IL-17 in the lymphoid compartment of aged skin

Lymphoid cells in the mouse dermis include T cells (CD4<sup>+</sup>, CD8<sup>+</sup>,  $\gamma\delta$  T cells and regulatory T (T<sub>reg</sub>) cells), ILCs and natural killer (NK) cells (Fig. 3a, left). These cells scan for tissue damage and perform immune surveillance in steady state, and also trigger an inflammatory response during wound healing and tumorigenesis<sup>38</sup>. The proportion of  $\gamma\delta$  T cells and CD4<sup>+</sup>T<sub>H</sub> cells increased in aged dermis (Fig. 2a and Extended Data

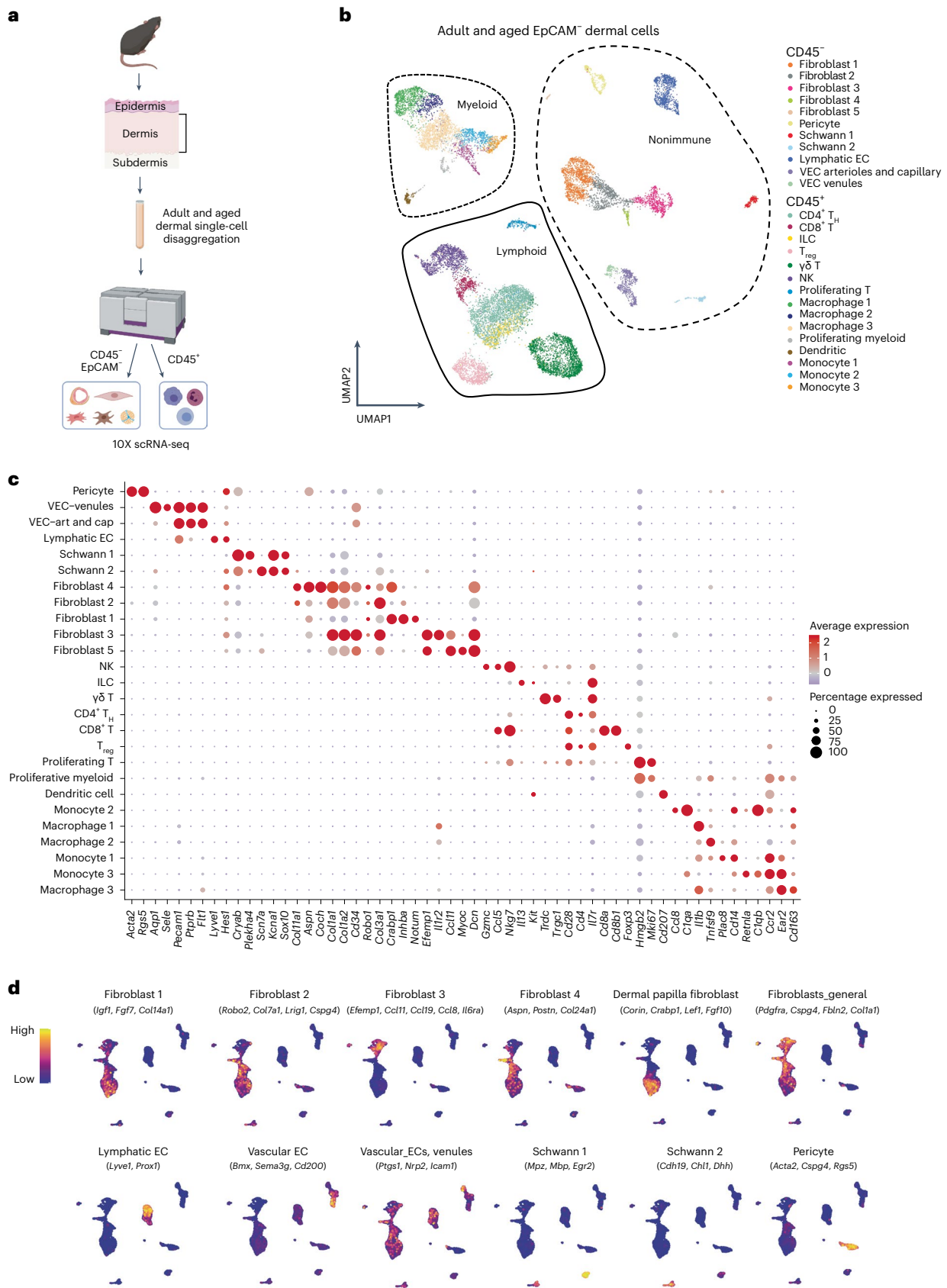


**Fig. 1 | Dermal cell characterization by 10X scRNA-seq. a**, Workflow used to obtain dermal cells of adult and aged mouse back skin. Single-cell suspensions were enriched separately for EpCAM $^-$ CD45 $^-$  and CD45 $^+$  cells by FACS. Transcriptomes of sorted single cells were then analyzed by 10X scRNA-seq. For CD45 $^+$  cells,  $n = 7$  mice for the adult group and  $n = 4$  mice for the aged group, with three technical replicates; for CD45 $^-$ EpCAM $^-$  cells,  $n = 2$  mice for the control

group and  $n = 2$  mice for the aged group, with two technical replicates. Created with [BioRender.com](https://www.biorender.com). **b**, UMAP visualization of all adult and aged dermal cells analyzed by 10X scRNA-seq. **c**, Dot plot showing discriminatory markers for each cell type, subtype and state found in **b**. **d**, UMAP visualization of nonimmune cell subtype-specific signatures. EC, endothelial cells; VEC, vascular endothelial cells.

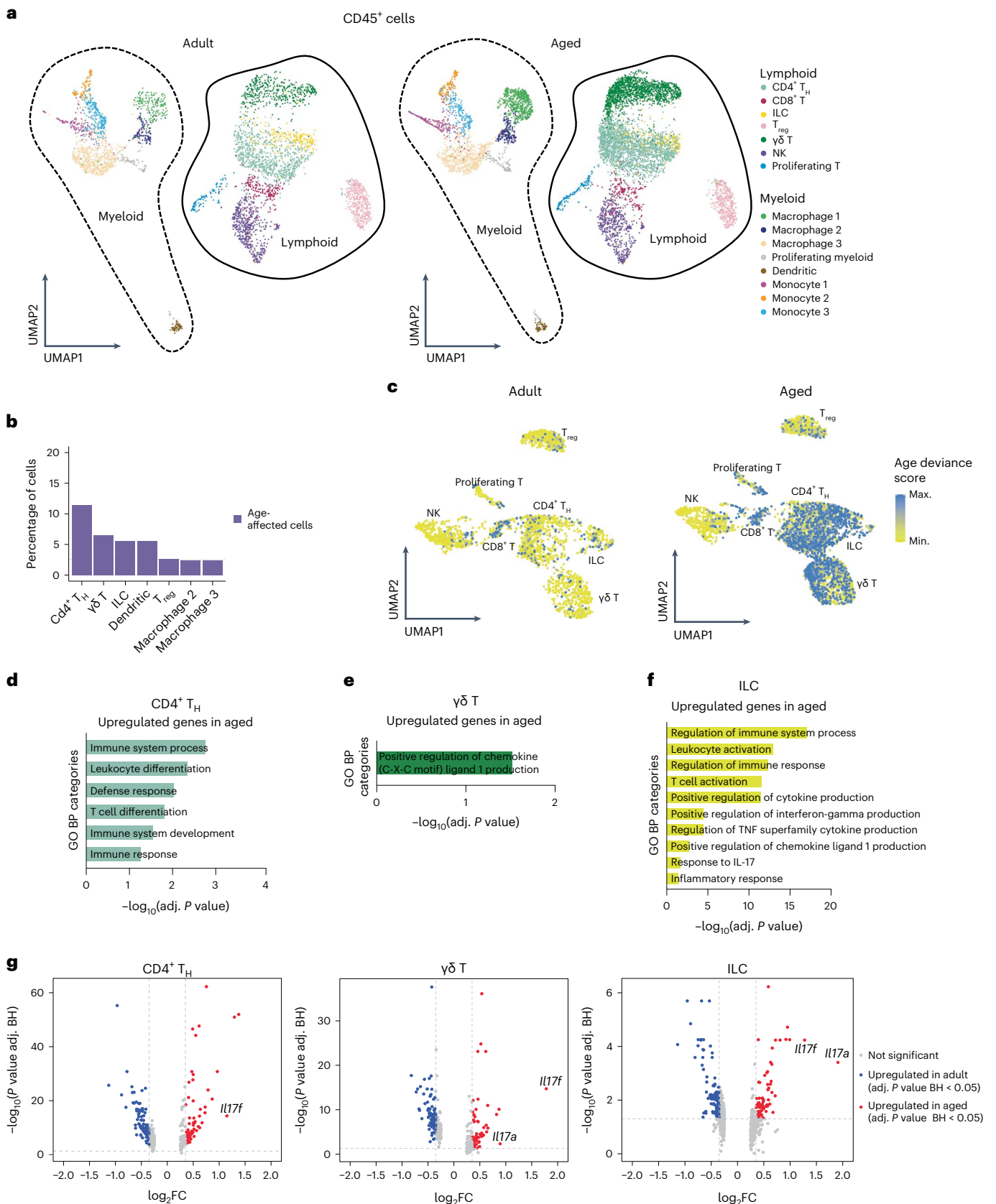


**Fig. 2 | Lymphoid immune cell subsets show increased IL-17A/F-related signaling.** **a**, UMAP representation of immune (CD45<sup>+</sup>) cells. **b**, Bar plot with the percentage of cells affected by aging in each immune dermal cell type (only cell types with higher percentage are shown here, for visual clarity). **c**, UMAP showing age-deviance score in adult (left) and aged (right) dermal lymphoid cells. **d–f**, Plots of selected GO categories in biological processes (BP) analysis for

genes upregulated during aging in CD4<sup>+</sup> T<sub>H</sub> cells (**d**), γδ T cells (**e**) and ILCs (**f**). The x axis represents  $-\log_{10}$  of the adjusted *P* value for each depicted GO category. **g**, Volcano plots showing differentially expressed genes between aged and adult CD4<sup>+</sup> T<sub>H</sub> cells, γδ T cells and ILCs. *Il17a* and *Il17f* are highlighted whenever found to be differentially expressed in a statistically significant manner between ages. BH, Benjamini–Hochberg; FC, fold change.

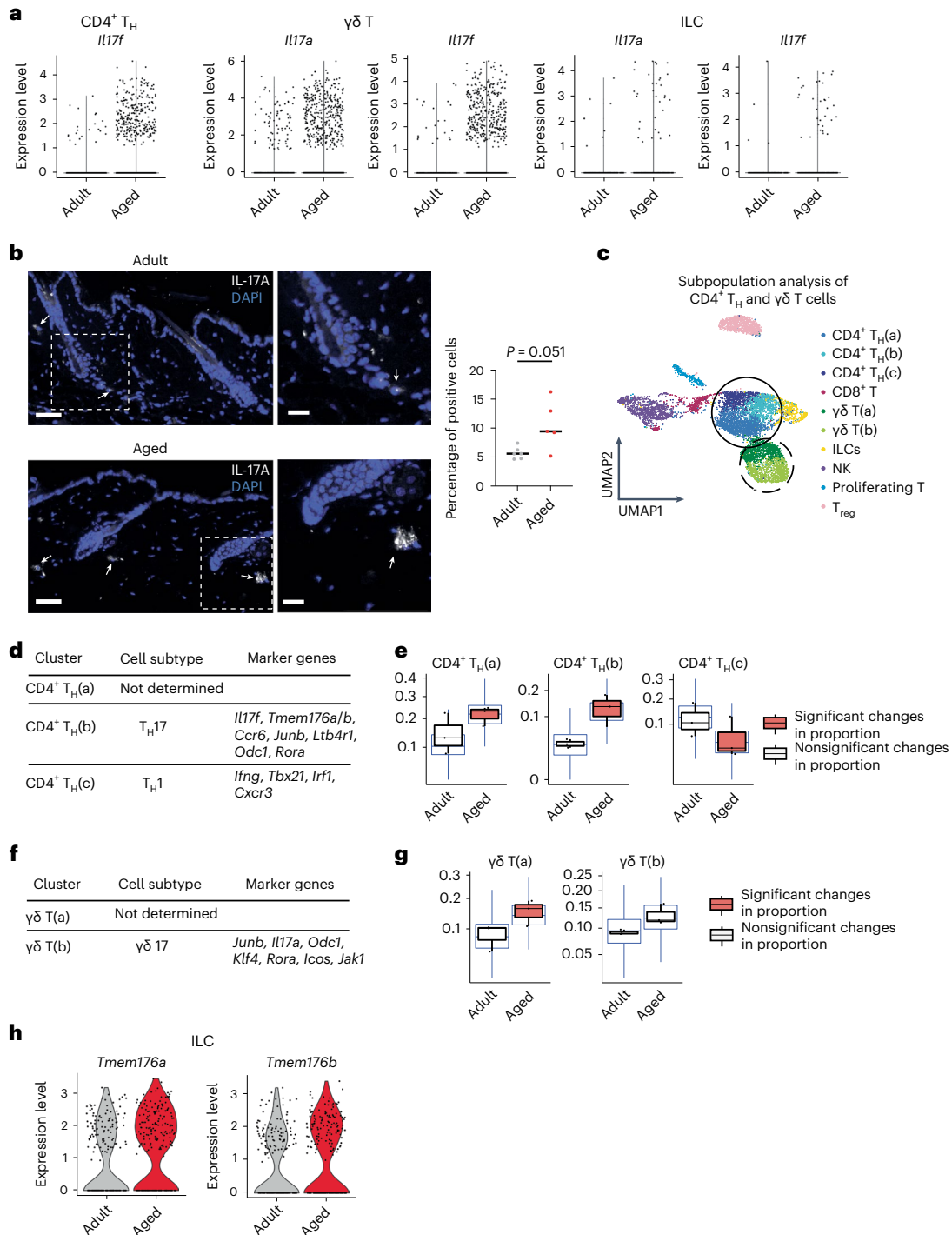


**Fig. 3 | Lymphoid cells skew towards an IL-17-expressing phenotype in aging.**

**a**, Violin plots comparing the expression values of *IL17a* and *IL17f* in aged and adult  $CD4^+ T_H$  cells,  $\gamma\delta T$  cells and ILCs. **b**, Immunofluorescence staining of IL-17A in adult (upper left) and aged (lower left) mouse back skin. Scale bars, 50  $\mu m$ . Insets, higher-magnification images focusing on the dermis (right). Scale bars, 20  $\mu m$ . White arrows indicate positive cells. For enhanced visualization, brightness and contrast were adjusted on these images.  $n = 6$  adult mice and  $n = 5$  aged mice collected in two independent experiments. Quantification is presented as the percentage of dermal positive cells. **c**, UMAP representation of subclustering of previously described  $CD4^+ T_H$  cell and  $\gamma\delta T$  cell clusters. Three new clusters of  $CD4^+ T_H$  cells were found ( $CD4^+ T_H(a-c)$ ), shown here in blue and circled by the continuous line; and two new clusters of  $\gamma\delta T$  cells were found ( $\gamma\delta T(a)$  and  $T(b)$ ), in green and circled by the dashed line. **d**, List of relevant markers discriminating subclusters belonging to specific  $CD4^+ T_H$  cell subtypes. **e**, Boxplots depicting changes in the proportion of  $CD4^+ T_H$  cell subclusters between aged and adult dermis, performed with *scompt*<sup>51</sup> and obtained using scRNA-seq data. Error

bars indicate 95% credible intervals and center line is the median. Black boxplots represent the observed data while blue ones indicate the posterior predictive check of the model. Boxes colored orange indicate statistically significant differences in cell proportion between conditions (FDR < 0.025 using Benjamini-Hochberg procedure to control for multiple testing). **f**, List of relevant markers discriminating subclusters belonging to specific  $\gamma\delta T$  cell subtypes. **g**, Boxplots depicting changes in the proportion and  $\gamma\delta T$  cell subclusters between aged and adult dermis, performed with *scompt*<sup>51</sup> and obtained using scRNA-seq data. Error bars indicate 95% credible intervals and center line is the median. Black boxplots represent the observed data while blue ones indicate the posterior predictive check of the model. Boxes colored orange indicate statistically significant differences in cell proportion between conditions and red triangles mark outliers. **h**, Violin plots showing expression values of *Tmem176a* and *Tmem176b* in comparison of adult and aged ILCs. **e, g**, Where differences in cell proportion between ages were significant, the boxplot is marked in orange.

Fig. 3b). We also confirmed that there was a higher frequency of CD4<sup>+</sup> cells by immunostaining the dermis of aged mice (Extended Data Fig. 3e). Accordingly,  $\gamma\delta$  T cells, CD4<sup>+</sup> T<sub>H</sub> cells and ILCs presented the most pronounced transcriptomic changes with age from all cell types analyzed (Fig. 2b,c).

Focusing on these lymphoid populations, aged CD4<sup>+</sup> T<sub>H</sub> cells,  $\gamma\delta$  T cells and ILCs expressed much higher levels of inflammatory genes than their adult counterparts (Fig. 2d–f and Supplementary Tables 2 and 3). The proinflammatory cytokine interleukin 17 (IL-17) family members *Il17a* and *Il17f* were among the most strongly upregulated genes in these cell types (Fig. 2g). There are six IL-17 members, IL-17A–IL-17F, all of which signal via binding to the IL-17R family of receptors. The highly homologous cytokines IL-17A and IL-17F bind as homo- or heterodimers to IL-17RA and IL-17RC receptors<sup>40</sup>. The IL-17 family of cytokines intervene in tissue repair and host defense and also have pathogenic roles in autoimmune and chronic inflammatory diseases<sup>40</sup>. Importantly, therapeutic inhibition of aberrant IL-17A and IL-17F activities is used as treatment for skin diseases such as psoriasis and other autoimmune conditions<sup>41–44</sup>. Notably, during aging there is a polarization of circulating CD4<sup>+</sup> T<sub>H</sub> cells towards an IL-17-expressing phenotype and, in mice,  $\gamma\delta$  T cells also show this skew in peripheral lymph nodes<sup>45–47</sup>. However, whether these changes affect peripheral tissue aging is unknown.

The increase in expression of *Il17a* and *Il17f* was restricted to these specific aged lymphoid cell types (Extended Data Fig. 4a). By contrast, expression of the receptors that bind these cytokines specifically (*Il17ra* and *Il17rc*) remained mostly unaltered across all cell types during aging (Extended Data Fig. 4a). The upregulation of *Il17a* and *Il17f* in CD4<sup>+</sup> T<sub>H</sub> cells,  $\gamma\delta$  T cells and ILCs during aging was due to increased expression in individual cells (Fig. 3a and Supplementary Table 2), suggesting that there was a polarization towards an IL-17-expressing phenotype. We also detected, by immunostaining, a higher proportion of IL-17A-positive cells in aged mouse back skin dermis (Fig. 3b). Furthermore, we analyzed *IL17A* and *IL17F* expression in adult and aged human dermis by fluorescent in situ hybridization (FISH) to determine whether this upregulation prevailed in other species. We observed a clear trend towards a higher (although not statistically significant) percentage of *IL17A*- and *IL17F*-positive cells in aged dermis compared with adult dermis. This confirms that our results in mouse skin are, to some extent, also observed in human skin (Extended Data Fig. 4b).

In our 10X scRNA-seq data, zooming in on the CD4<sup>+</sup> T<sub>H</sub> cell cluster further revealed three subclusters with specific marker gene expression (Fig. 3c,d and Supplementary Table 1). While the CD4<sup>+</sup> T<sub>H</sub>(a) cell cluster could not be assigned to any specific T<sub>H</sub> cell subtype, the CD4<sup>+</sup> T<sub>H</sub>(c) cell cluster showed markers usually expressed by T<sub>H</sub>1 cells such as *Irfng*. The CD4<sup>+</sup> T<sub>H</sub>(b) cell cluster showed markers compatible with their being bona fide T<sub>H</sub>17 cells, including *Il17f*, *Rora*, *Tmem176a/b*, *Ccr6* and *Junb* among others<sup>48–50</sup> (Fig. 3d). This cell subtype, CD4<sup>+</sup> T<sub>H</sub>(b) cells (T<sub>H</sub>17 cells), showed an increase in abundance in aged dermis compared with control adult skin (Fig. 3e). Accordingly, the presence of CD4<sup>+</sup> T<sub>H</sub>(c) cells (T<sub>H</sub>1 cells) was decreased in aged dermis (Fig. 3e), pointing again to a skewing of dermal CD4<sup>+</sup> cells towards a T<sub>H</sub>17 cell phenotype during aging.

Similar to T<sub>H</sub> cells,  $\gamma\delta$  T cells could also be further clustered into two subpopulations (Fig. 3c,f and Supplementary Table 1). The  $\gamma\delta$  T(b) cell cluster expressed markers compatible with  $\gamma\delta$  T17 cells, as indicated by the expression of *Il17a*, *Rora*, *Junb* and *Jak1* among others<sup>50</sup>, whereas the  $\gamma\delta$  T(a) cell cluster could not be assigned to any specific  $\gamma\delta$  T cell subtype (Fig. 3f). Both  $\gamma\delta$  T cell clusters were more abundant in aged skin although only the  $\gamma\delta$  T(a) cell subcluster was significantly increased, showing an increased presence of IL-17-expressing  $\gamma\delta$  T cells in aged mouse skin (Fig. 3g).

ILCs are crucial for the development of psoriatic pathogenesis through sustained increased secretion of IL-17 (ref. 51). Our analysis also showed a marked increase in the expression of genes associated with

the switch to ILC subtype 3 (refs. 51,52), such as *Il17a*, *Il17f*, *Tmem176a* and *Tmem176b* in aged skin (Fig. 3a,h and Supplementary Table 2).

### Inhibition of IL-17A/F prevents age-related inflammation

We next sought to determine whether increase in the expression of *Il17a* and *Il17f* contributes to the general proinflammatory state of aged skin. Treatment with antibodies that neutralize IL-17A and IL-17F (anti-IL-17A/F) is currently used as a therapy for patients with inflammatory and autoimmune diseases such as psoriasis<sup>44</sup>. We therefore blocked IL-17 signaling by systemic administration of anti-IL-17A/F (or an IgG isotype control) in aging mice (73 weeks old) for 12 weeks (Fig. 4a). We then isolated dermal cells by FACS and performed 10X scRNA-seq, following a previous workflow (Fig. 1a). In total, 16,975 CD45<sup>+</sup> cells and 33,262 CD45<sup>+</sup> EpCAM<sup>+</sup> cells were analyzed with the same bioinformatics pipeline as the aged sample analysis. We further verified batch effect, good sample mixing and representation of all replicates although no batch effect correction was deemed necessary for these samples (Extended Data Fig. 5a,b). We clustered the cells and confirmed that the same cell types were detected (Fig. 4b).

**Nonimmune dermal cells.** Nonimmune dermal clusters did not show major changes in gene expression following IL-17A/F inhibition. However, neutralization of IL-17A/F activity decreased the abundance of fibroblast 3 cells, previously described as the proinflammatory type of fibroblast (Extended Data Fig. 6a, bottom). This suggests that, even though the transcriptome of these cells is not markedly altered, they still responded to the blocking treatment.

**Immune cells.** Myeloid cells respond to IL-17 signaling in inflammatory situations, activating the expression of more proinflammatory cytokines<sup>53</sup>. The upregulation of proinflammatory cytokines (such as *Il1b* in clusters monocyte 1, macrophage 2 and dendritic cells) that we observed in aged cells was attenuated following neutralization of IL-17A/F signaling (Extended Data Fig. 6b and Supplementary Tables 4 and 5). We also observed a general decrease of proinflammatory genes in the monocyte 1 cluster (Extended Data Fig. 6c), which we previously identified as proinflammatory monocytes, although no significant changes in proportion were detected (Extended Data Fig. 6a).

Anti-IL-17A/F treatment led to no differences either at the transcriptomic level or in cell proportion analysis on lymphoid cells (Supplementary Table 4 and Extended Data Fig. 6a).

Consequently, our results indicate that blockade of IL-17A/F signaling affects certain dermal cell populations in a cell type-specific manner.

### Delay in epidermal aging traits following IL-17A/F blockade

We next investigated whether anti-IL-17A/F treatment would also ameliorate age-associated traits in keratinocytes. Sustained inflammation in aged epidermis is thought to affect epidermal stem cell fitness, potentially by reducing their regenerative function<sup>2,10,13,17</sup>. Bulk RNA-seq of aged and adult epidermal cells confirmed that the expression of proinflammatory cytokines and chemokine signaling increases in aged skin (Extended Data Fig. 7a and Supplementary Table 6). Importantly, IL-17A/F blockade reduced expression of cytokine-related signaling and chemotactic genes, including *Ccl5*, *Cxcr3* and *Xcl1*, as well as downregulated genes involved in proinflammatory processes including *Tnf* (Fig. 4c, Extended Data Fig. 7b and Supplementary Table 6). Concomitant to this, there was an increase in the expression of genes related to healthier wound healing such as *Wnt7a*<sup>54</sup> (Fig. 4c, Extended Data Fig. 7b and Supplementary Table 6).

### Youthful skin traits increase following IL-17A/F blockade

**Cornified layer thickness.** A well-defined age-related phenotype in the epidermis is the increased thickness of the cornified layer<sup>2</sup>. Indeed, the thickness of this layer doubled in aged as compared with adult mice

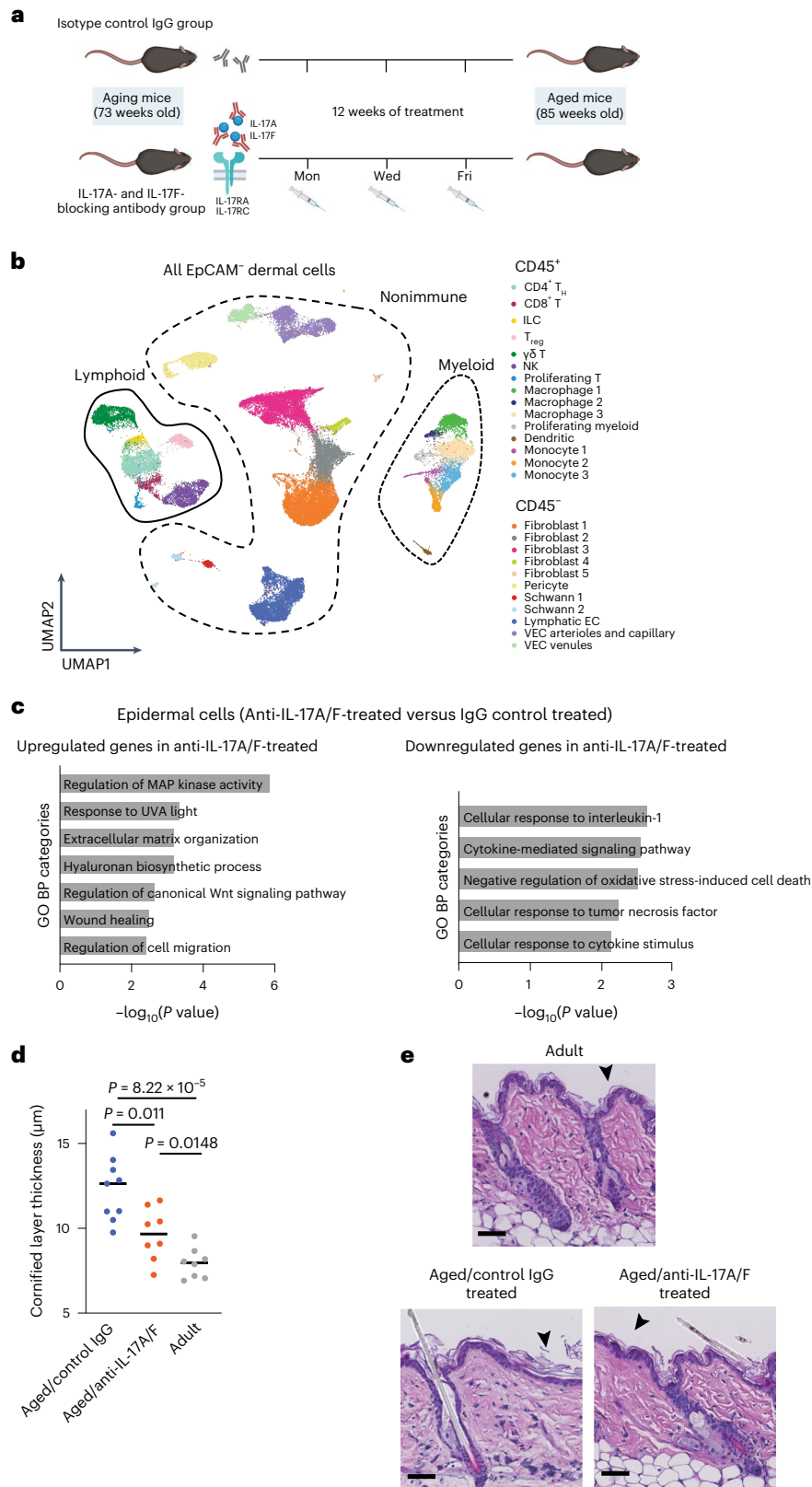


**Fig. 4 | Blockade of IL-17A/F function in aging mice leads to a delay in age-associated skin traits. a**, Diagram showing anti-IL-17A/F treatment workflow. Created with [BioRender.com](https://www.biorender.com). **b**, UMAP representation of all CD45<sup>+</sup> and CD45<sup>-</sup> EpCAM<sup>-</sup> cells analyzed by 10X scRNA-seq obtained following IL-17A/F blockade. **c**, Plot of selected GO categories belonging to BP analysis for genes upregulated (left) and downregulated (right) after IL-17A/F-blocking treatment in epidermal cells. **d**, Dot plot showing quantification of cornified layer thickness in aged/IgG control, aged/anti-IL-17A/F-treated and adult mice. Each dot

represents the average of ten measurements per mouse ( $n = 8$  mice, collected in two independent experimental replicates pooled) performed on H&E stainings of skin sections. Horizontal lines represent the median of individual values per age and condition.  $P$  values were calculated by two-tailed Mann-Whitney  $U$ -test. **e**, Representative images of H&E staining of adult, aged/IgG control and aged/anti-IL-17A/F-treated mice. Scale bars, 50  $\mu$ m. Cornified layer thickness (black arrowheads) was measured using scaled images.

(Fig. 4d,e). In vivo systemic inhibition of IL-17 (using anti-IL-17A/F) in aging mice resulted in a thinner cornified layer compared with aged/IgG-treated control mice (Fig. 4d,e).

**Hair follicle growth.** Aged hair follicles show a lower capacity to enter the growing phase of the hair cycle (anagen)<sup>17</sup>. Anagen can be subdivided into phases that indicate how far the growth of the hair follicles has advanced<sup>55</sup>. As expected, hair follicles in our cohort of aged mice showed a delay in the anagen stage as compared with their adult counterparts at 8 days post epilation (Fig. 5a,b and Extended Data Fig. 7c). Although anti-IL-17A/F treatment in aged mice did not induce spontaneous anagen entry (Extended Data Fig. 7d), hair follicles of aged/anti-IL-17A/F-treated mice showed a faster pace in their anagen entry and progression almost identical to that in adult mice. This points towards a strong amelioration of the capacity of hair follicle stem cells to activate compared with aged/IgG-treated control mice (Fig. 5a,b and Extended Data Fig. 7c). Dermal papilla fibroblasts express secreted factors essential for hair follicle anagen entry, such as *RSPO3* (ref. 34). We observed higher *Rspo3* mRNA expression by FISH in aged/anti-IL-17A/F-treated mice compared with aged/IgG-treated control mice, although this difference was not statistically significant (Extended Data Fig. 7e). This suggests that dermal papilla fibroblasts could be more fit to regrow hair following IL-17A/F blockade.

**Transepidermal water loss.** The cornified layer confers impermeability to the skin due to the presence of crosslinked proteins and lipids, and is altered during the aging process<sup>12</sup>. When this layer is removed by mechanical means (for example, by tape stripping), the epidermal barrier becomes permeable (higher transepidermal water loss (TEWL)). Recovery of basal TEWL values after tape stripping is achieved in a few hours under homeostatic conditions. Nonetheless, the efficiency of recovery is affected by aging<sup>8,12,56</sup>. Accordingly, TEWL values recorded during the first 24 h after tape stripping showed a significant delay in aged/IgG-treated mice compared with adults (Fig. 5c and Extended Data Fig. 7f), but delayed barrier recovery was not as strong in aged/anti-IL-17A/F-treated mice when compared with aged/IgG-treated mice (Fig. 5c and Extended Data Fig. 7f). This shows an improvement in the barrier recovery of aged/anti-IL-17A/F-treated mice after sublesional injury to the cornified layer compared with their aged/IgG-treated counterparts.

**Wound healing.** Efficient wound healing requires a rapid tissue response for efficient re-establishment of the skin barrier. The dialog between dermal and epidermal cells is impaired during aging, leading to a delay in wound healing<sup>18,27</sup>. To test the impact of in vivo IL-17A/F blockade on wound healing we created a 5-mm wound on each flank of adult, aged/IgG control and aged/anti-IL-17A/F-treated mice. Wound closure did not show differences between age groups by macroscopic measurement of wound diameter in vivo throughout the ten post-wounding days (Extended Data Fig. 7g), as suggested by previous reports<sup>18</sup>.

After wounding, functional barrier regeneration is achieved by complete maturation of keratinocytes, including the enucleation of the upper layers of the epidermis (orthokeratosis)<sup>57,58</sup>. Nevertheless, incomplete maturation of keratinocytes can occur in aberrantly healing and chronic wounds where immature nucleated cells can populate the uppermost layers of the epidermis (parakeratosis)<sup>59</sup>. Importantly, when we assessed the epidermal maturation status of the re-epithelized area 10 days after injury we observed that, in adult mice, most of the new epidermis was composed mainly of orthokeratotic epithelium (that is, enucleated cells in the cornified layer). Conversely, in the aged/IgG-treated control mice the presence of parakeratosis in the majority of wounds points to a delay in epidermal maturation and incorrect barrier recovery (Fig. 5d,e) previously reported for aged wounds<sup>59</sup>. In aged/anti-IL-17A/F-treated mice the epithelization maturation state

10 days after wounding reached a degree intermediate between adult and aged/IgG-treated control wounds (Fig. 5d,e). Moreover, in the dermis a paramount event for correct wound healing is the maturation process of granulation tissue—newly formed blood vessels, immune cells and fibroblasts that help close the wound<sup>60</sup>. As wound healing progresses the granulation tissue matures towards a fibrotic tissue that will eventually form a scar. We observed immature granulation tissue in the majority of aged/IgG-treated control wounds 10 days after wounding. This trend was partially reversed in adults and intermediate maturation was observed in most of these wounds (Fig. 5d,f). The blockade of IL-17A/F signaling in aged mice allowed the progression of granulation tissue maturation to an adult-like state (Fig. 5d,f).

The amelioration of these parameters during wound healing suggests that short-term in vivo blockade of IL-17A/F signaling in aging mice aids the wound-healing process at two different levels: it helps in efficient maturation of both the re-epithelized area and subjacent granulation tissue. To summarize the foregoing, aberrant IL-17A/F signaling is at the hinge between dermal and epidermal cells and its neutralization results in a synergy that delays age-associated skin traits.

### IL-17A/F–NF- $\kappa$ B signaling is key in epidermal aging

Epidermal cells are responders to IL-17A and IL-17F in the skin<sup>42</sup>. Once IL-17 receptors IL-17RA and IL-17RC become activated, they signal through downstream transcription factors such as the canonical nuclear factor  $\kappa$ -light-chain-enhancer of activated B cells (NF- $\kappa$ B)<sup>40</sup>. Because tight regulation of NF- $\kappa$ B activity is needed for correct epidermal homeostasis and defense response<sup>38</sup>, we hypothesized that upregulation of IL-17A/F-dependent inflammation-related genes in aged epidermis might rely on NF- $\kappa$ B transcriptional activity. To test this, we performed chromatin immunoprecipitation followed by sequencing (ChIP-seq) for p65 (encoded by *Rela*) in epidermal cells from aged/IgG-treated control, aged/anti-IL-17A/F-treated and adult mice. We annotated the peaks to their closest gene, filtered out those not associated with protein-coding genes and analyzed their biological function by Gene Ontology (GO) term analysis (Extended Data Fig. 8a and Supplementary Table 7).

Genes bound by p65 in the aged/control IgG-treated samples showed an increase in inflammation-related functions when compared with those in adults, as reflected by the higher statistical significance of inflammation-related categories in GO analysis (Fig. 6a). This was accompanied by the presence of p65 in regulatory areas of specific proinflammatory genes in aged/IgG-treated control samples, such as *Il9* and *Crlf2*, which have been described as relevant in immune responses<sup>61,62</sup> (Fig. 6b). After in vivo blockade of IL-17A/F activity in aging mice, this age-associated inflammatory trend was reversed (Fig. 6a,b). Nonetheless, this effect was only partial because some of these inflammatory genes remained bound by p65 following anti-IL-17A/F treatment (Extended Data Fig. 8b,c). This suggests that the effect of in vivo anti-IL-17A/F treatment in aging mice, although sufficient to delay many aging-related skin traits, may be acting only partially in a p65-binding-dependent manner.

In addition, we observed that binding of p65 to the regulatory areas of certain genes relevant to epidermal homeostasis was lost during aging (Fig. 6c). Such is the case for *Eupl1* and *Krt14* (which encode envoplakin and keratin 14, respectively), essential in skin barrier function and stem cell maintenance, respectively<sup>63,64</sup> (Fig. 6d). Importantly, binding of p65 to those genes was recovered following IL-17A/F in vivo blockade, suggesting that decreased IL-17A/F activity might redirect p65 to genes essential for epidermal function that are lost during aging (Fig. 6d). This effect was also partial, because other genes important for epidermal development and maturation, such as *Dll1* (ref. 65), remained unbound in aged/anti-IL-17A/F-treated epidermis (Extended Data Fig. 8d).

Thus, we have found that p65/NF- $\kappa$ B is an IL-17A/F-responsive transcription factor in epidermal cells that accounts for part of the



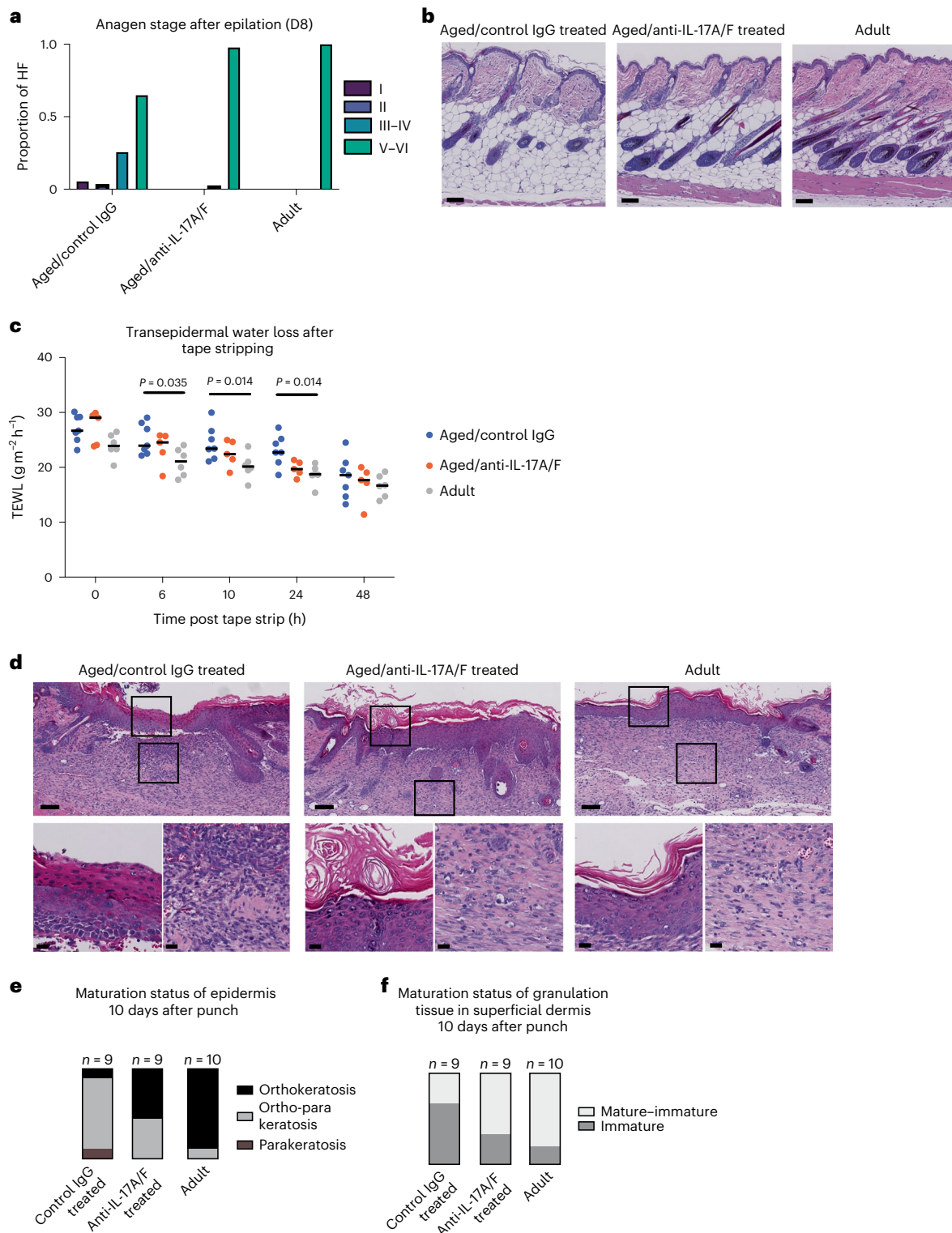


**Fig. 5 | Decreased skin age-associated traits following IL-17A/F blockade.**

**a**, Quantification of anagen stages in mouse back skin at 8 days (D8) post epilation of aged/IgG control, aged/anti-IL-17A/F-treated and adult mice;  $n = 6$  mice per condition. **b**, Details of H&E staining of epilated back skin samples at 8 days post epilation. Scale bars, 100  $\mu\text{m}$ . This experiment was performed in two independent technical replicates with similar results, pooled in the analysis shown here. **c**, Plot depicting transepidermal water loss values ( $\text{g m}^{-2} \text{h}^{-1}$ ) after tape stripping during 48 h in aged/IgG control ( $n = 7$ ), aged/anti-IL-17A/F-treated ( $n = 5$ ) and adult ( $n = 6$ ) mice. This experiment was performed in two independent technical replicates with similar results, pooled in the analysis shown here.  $P$  values were calculated by two-tailed Mann-Whitney  $U$ -test.

**d**, Top, representative images of H&E staining of wound tissue 10 days post wound generation. Scale bars, 100  $\mu\text{m}$ . Bottom, zoomed-in views of boxed areas in top panels showing details of epidermis and dermal granulation tissue. Scale bars, 20  $\mu\text{m}$ . This experiment was performed in three independent technical replicates with similar results, pooled in the analysis shown here. **e**, Boxplot showing the maturation status of epidermis in aged/IgG control, aged/anti-IL-17A/F-treated and adult mice, qualified by the presence or absence of nuclei in the cornified layer (parakeratosis versus orthokeratosis) at 10 days post wounding. **f**, Boxplot showing the maturation status of granulation tissue in the superficial dermis in aged/IgG control, aged/anti-IL-17A/F-treated and adult mice at 10 days post wounding. HF, hair follicle.

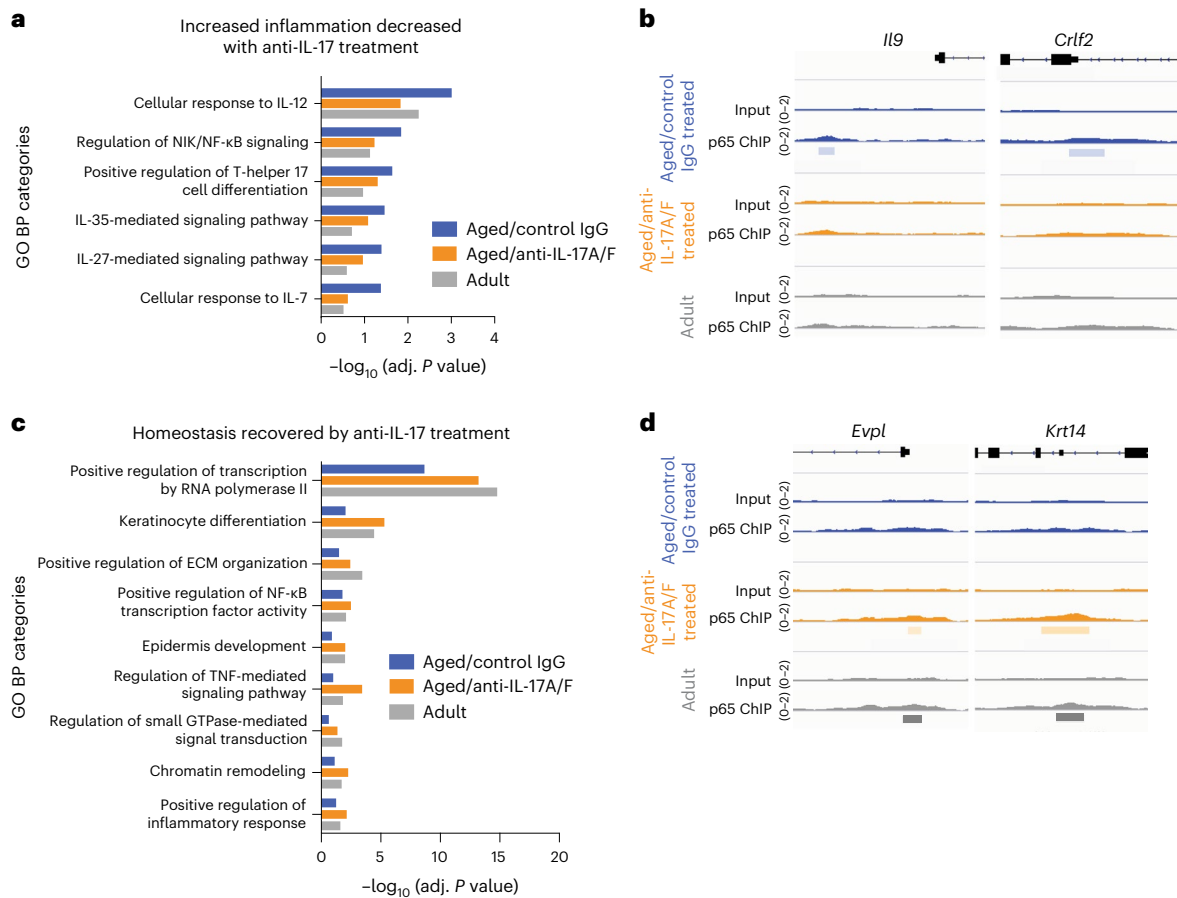


**Fig. 6 | IL-17 signaling is partially transduced by p65/NFκB signaling in epidermal cells. a**, Plot comparing the adjusted  $P$  values of selected inflammation-related GO categories of genes bound by p65 in aged/IgG control, aged/anti-IL-17A/F-treated and adult mice. **b**, Representative images of genes belonging to inflammation-related GO categories showing binding of p65 to their

regulatory areas. **c**, Plot comparing adjusted  $P$  values of selected homeostasis-related GO categories of genes bound by p65 in aged/IgG control, aged/anti-IL-17A/F-treated and adult mice. **d**, Representative images of genes belonging to the selected epidermal homeostasis-related GO categories showing binding of p65 to their regulatory areas.

change towards a more proinflammatory and less homeostatic gene expression in aging.

## Discussion

During aging, tissue-specific alterations in the niche synergize with stem cell-intrinsic changes to contribute to the development of age-associated traits<sup>17,66–68</sup>. Aging has been proposed to drive a tissue-dependent proinflammatory microenvironment that perturbs adult stem cell behavior<sup>69–72</sup>. Infiltration of immune cells into the stem cell niche<sup>69</sup>, or a transcriptional switch of stem cells, contributes to this proinflammatory environment that negatively feeds back to their own fitness<sup>70</sup>. Here we have characterized the effects of the proinflammatory cytokine IL-17 on skin aging. Our results show that elevated IL-17 signaling, secreted by aged dermal CD4<sup>+</sup> T<sub>H</sub> cells, γδ T cells and ILCs, orchestrated many of the age-associated tissue dysfunctions by exertion of pleiotropic effects. IL-17-mediated signaling is heavily linked to the development of chronic inflammatory and autoimmune diseases<sup>42,46,73</sup>. In the skin, these diseases include psoriasis, pemphigus and alopecia areata<sup>43</sup>. Even if none of the clinical signs of these diseases are common with physiological aging, they share an increased aberrant IL-17-based signaling that impedes correct skin function. Our results strongly suggest that, intriguingly, the local environment of the aged skin resembles a low-level but persistent state of chronic inflammation, with deficient permeability and impaired wound healing that is reminiscent of what occurs in serious skin diseases such as psoriasis. Consequently, anti-IL-17 therapies, already approved for treatment

of psoriasis, might be repositioned to other age-associated ailments such as excessive skin dryness or difficulty in repairing damaged skin in the elderly.

## Methods

### Mouse handling and husbandry

Mice were housed under a regimen of 120h/12-h light/dark cycles and specific-pathogen-free conditions. The temperature of the animal facility was maintained between 20 and 24 °C and humidity ranged from 45 to 65%. Animals were handled following the ethical regulations and guidelines of Scientific Park of Barcelona and the Government of Catalunya. All procedures were evaluated and approved by the Ethical Committee for Animal Experimentation of the Government of Catalunya (approval reference no. 10712). All mice used were from the C57BL/6J strain. Aged mice were either bred in-house or were retired C57BL/6J breeder females purchased from Charles River, and were kept until the desired age in the animal facility at Barcelona Science Park. Control adult mice were either bred in-house or purchased from Charles River to generate matching cohorts. Mostly female mice were used due to this fact, and also to differences in skin-digesting efficiency between sexes, because longer male skin digestion times are required and this reduced the survival of sorted dermal cells, skewing the results towards the most resilient cell types. For experiments that did not require enzymatical digestion of the dermis, both males and females were used. Mice were always killed during darkness, to coincide with their active phase. Aged mice were between 80 and 90 weeks of age

and adult mice were between 17 and 25 weeks of age. Mice with signs of skin inflammation (dermatitis, wounds or redness) were excluded from the experiments to avoid interference with the results.

### Epidermal and dermal cell isolation for genomics analysis

Mice were killed and whole-torso skin was removed as rapidly as possible. Hypodermal fat was removed by scalpel and, after two washes in PBS, skins were floated (dermal side down) in dispase II solution (5 mg ml<sup>-1</sup>; no. D4693, Sigma-Aldrich) in PBS for 30–40 min at 37 °C. Epidermis was removed by scalpel. For dermal cell isolation, dermis was mechanically dissociated using a McIlwain Tissue Chopper (The Mickle Laboratory Engineering Co.) and then further digested in Liberase TM (6.5 Wünsch units per reaction, Roche) diluted in DMEM (no. 41965, Thermo Fisher Scientific) for 20–30 min at 37 °C with gentle agitation. Afterwards, DNase I (1 mg ml<sup>-1</sup>; no. DN25, Sigma-Aldrich) was added to the mix with incubation for 15 min at 37 °C without agitation. Digested dermis was first strained through a 100- $\mu$ m strainer and then through a 40- $\mu$ m strainer, to obtain single-cell suspensions.

### RNA-seq

For bulk RNA-seq of adult and aged, and aged/control IgG-treated and anti-IL-17A/F-treated, mice, four mice were used per condition. Cells in single-cell suspensions were frozen in 1 ml of Trizol (Invitrogen) for posterior RNA isolation. RNA was extracted from epidermal cell pellets frozen in Trizol using the RNeasy Mini Kit (Qiagen) and further processed for mRNA-seq with Illumina sequencing technology.

### Flow cytometry and cell sorting (yielding CD45<sup>+</sup>, CD45<sup>-</sup> EpCAM<sup>-</sup>)

For 10X scRNA-seq, single-cell dermal suspensions were incubated with CD45-APC (clone 30-F11, 1:100, no. 559864 BD Biosciences) and EpCAM-PE (clone G8.8, 1:200, no. 552370 BD Biosciences) for 45 min on ice. After two washes in PBS, cells were resuspended in 2  $\mu$ g ml<sup>-1</sup> DAPI (no. 32670, Sigma-Aldrich) to stain DNA. These were then analyzed using a BD FACSAria Fusion flow cytometer with FACSDiva software v.8.0.1, in which CD45<sup>+</sup> cells were retained and EpCAM<sup>-</sup> cells excluded. For flow cytometry analyses, FlowJo v.10.0.8.r1 was used.

### In vivo anti-IL-17A/F-neutralizing treatment

Cohorts of aging (73-week-old) mice were randomly distributed into two groups and were treated with either (1) a mixture of 105  $\mu$ g of anti-IL-17A (clone 17F3, no. BE0173, BioXCell) and 105  $\mu$ g of anti-IL-17F (clone MM17F8F5.1A9, no. BE0303, BioXCell) or (2) 210  $\mu$ g of control IgG1 (clone MOPC-2, no. BE0083, BioXCell). Injections of 100  $\mu$ l of antibody solution in PBS were administered intraperitoneally and performed three times per week during the dark cycle at the same time of day (2–3 h into the dark phase). After 12 weeks of treatment, mice were either (1) killed to obtain samples of either dermal cells for 10X scRNA-seq or epidermal bulk RNA-seq of the epidermis and histology analysis or (2) used to measure skin aging traits.

### Epilation

Adult ( $n = 6$ , 18–20-week-old), aged/IgG control and aged/anti-IL-17A/F ( $n = 6$ , 85-week-old) female mice treated for 12 weeks with either IgG control ( $n = 6$ , 85-week-old) or anti-IL-17A/F were used ( $n = 6$ , 85 weeks old). Mice were anesthetized using a mixture of ketamine (75 mg kg<sup>-1</sup> body weight) and medetomidine (1 mg kg<sup>-1</sup>) by intraperitoneal injection. Buprenorphine (0.05 mg kg<sup>-1</sup>) was injected subcutaneously as analgesic and anti-inflammatory treatment. An area of about 2–3 cm<sup>2</sup> of back skin was epilated using wax papers until hair was completely removed (usually two or three rounds of waxing). Atipamezole (1 mg kg<sup>-1</sup>) was injected to reverse anesthesia, and mice were left on heating pads until completely recovered. Mice were housed individually to avoid scratching and contact of the epilated areas. Animal health status was monitored daily. After 8 days post hair removal, mice were

killed and images of shaved back skin captured. Samples of back skin were taken, fixed in neutral buffered formalin (10%) for 3 h at room temperature, dehydrated and embedded in paraffin blocks for later histological assessment.

### Wounding and wound-healing experiments

Adult mice ( $n = 15$ , 18–20 weeks old) and aged mice ( $n = 14$ , 85 weeks old) treated for 12 weeks with IgG control as previously described, and aged male and female mice ( $n = 15$ , 85 weeks old) treated for 12 weeks with anti-IL-17A/F, were used. For the IL-17-blocked group, IL-17A/F-blocking injections were stopped 1 week before starting the wound-healing assay to normalize IL-17 endogenous activity and separate the role of this cytokine in wound healing<sup>74</sup> from its role during aging.

Mice were anesthetized using 3–4% isoflurane, and buprenorphine (0.05 mg kg<sup>-1</sup>) was injected subcutaneously for analgesia. Body temperature of the animals was maintained by placing them on a heating mat covered by a sterile surgical drape throughout the process. Hair was shaved in the back region and the area sterilized with 10% povidone-iodine in distilled H<sub>2</sub>O solution. Two skin biopsies were carried out per animal, one on each flank using a 5-mm-diameter sterile, disposable circular biopsy punch (5 mm diameter, Kai medical, no. BP-50F). Sharp scissors were used to specifically dissect the skin layer biopsy after using the punch, to avoid affecting other underlying tissue. Mice were placed on warm pads until fully recovered from anesthesia and then housed individually throughout the entire experiment. Wound areas were macroscopically assessed by daily measurement of length and width using a digital caliper (Traceable Digital Caliper). For wound area analysis, measurements of two wounds per animal were averaged. All wounds were collected, fixed in neutral buffered formalin (10%) for 3 h at room temperature, dehydrated and embedded in paraffin blocks for later histological assessment.

### Barrier recovery measurement

Barrier integrity was assessed by measurement of TEWL, a parameter that measures water evaporation directly on the skin surface using a probe (Tewameter TM Nano, Courage+Khazaka). The animals used included adult ( $n = 6$ , 18–20-week-old), aged/IgG control ( $n = 7$ , 85-week-old) and aged/IL-17A/F-treated ( $n = 5$ , 85-week-old) female mice. Back skins were shaved 24 h before barrier disruption assay. Mice were anesthetized using 3–4% isoflurane and their temperature maintained constant at 37 °C by keeping them on a tightly regulated thermal plate during TEWL measurements. The mice were left to acclimate after induction of anesthesia and before starting tape stripping and measurements. All measurements were carried out at the same location by the same person, and room temperature and humidity were recorded. The order of data collection was randomized on the first occasion but was then replicated for each consequent measure.

The epidermal barrier was disrupted by tape stripping (Corneo-fix CF 20, Courage+Khazaka) and the number of tape strips adjusted according to mouse age to obtain TEWL > 20 g m<sup>-2</sup> h<sup>-1</sup> (ref. 75). A range of between six and ten strips was needed for adults, and 12–16 for aged/IgG controls and aged/anti-IL-17-treated mice. For TEWL measurements the probe was used according to the manufacturer's instructions. The probe was placed in each location of the skin surface being measured for 40 s before stabilization, each measurement lasting 1 min. TEWL probe measurements were carried out immediately after tape stripping ( $t_0$ ) and 6, 10, 24 and 48 h post tape stripping ( $t_6$ ,  $t_{10}$ ,  $t_{24}$ ,  $t_{48}$ , respectively). Two measurements per animal were recorded, and we averaged their TEWL value to obtain one single value per animal and per time point. Also, for consistency, the probe was placed at these same two locations for each consecutive measurement. The locations used for measurements were carefully selected to avoid areas where tape stripping had caused the appearance of small wounds, to prevent alteration of the actual barrier recovery values.

### Chromatin immunoprecipitation

Four independent mice per condition of adult, aged/IgG-treated control and aged/anti-IL-17A/F-treated were used for p65 chromatin immunoprecipitation sequencing (ChIP-seq). To isolate epidermal cells, the epidermal cell isolation protocol described below was followed (Epidermal and dermal cell isolation for genomics analysis). Instead of dispase II solution, 0.8% trypsin solution (trypsin 1:250, dissolved in PBS) was used to separate dermis from epidermis for 30–40 min at 37 °C. Around 30 million pelleted epidermal cells were used per reaction. The cells were crosslinked using Gold fixative (no. C01019027, Diagenode) following the manufacturer's directions. After two PBS washes, a second fixation was carried out in methanol-free 1% formaldehyde (no. 28908, Thermo Fisher Scientific) in MEM calcium-free medium with 10% calcium-chelated fetal bovine serum for 10 min with rotation. Glycine was then added to a final concentration of 125 mM to stop crosslinking, with incubation for 5 min under rotation. The pellet was washed twice with cold PBS and the cells then resuspended in 7.5 ml of swelling buffer (25 mM HEPES pH 7.9, 1.5 mM MgCl<sub>2</sub>, 10 mM KCl, 0.1% NP-40 supplemented with 1× protease inhibitors without EDTA). This cell suspension was homogenized 50 times with a Dounce homogenizer and tight pestle (no. 885302-0015, Kimble) and the extracts were centrifuged (3,000g, 5 min). Pelleted nuclear extracts were resuspended (in one-tenth of the volume used for the swelling buffer) in ChIP buffer (10 mM Tris-HCl pH 7.5, 150 mM NaCl, 1% Triton X-100, 5 mM EDTA, 0.5 mM DTT, supplemented with 0.2% SDS and 1× protease inhibitors without EDTA). This suspension was incubated for 15 min and then transferred to sonication tubes (no. C01020031, Diagenode). Sonication was carried out in 30 cycles of 30/30 min on/off at 4 °C (Bioruptor Pico, Diagenode) and the sonicated supernatant was centrifuged (14,000g, 10 min). The supernatant containing the chromatin was quantified for ChIP-seq.

For immunoprecipitation, 30 µg of chromatin was diluted with ChIP buffer without SDS to dilute the SDS concentration to 0.1% in all samples. Then, 4 µg ml<sup>-1</sup> anti-p65 (no. 8242, Cell Signaling Technology) was added and samples rotated overnight at 4 °C. Sepharose beads (no. 17-5280-01, Merck) were used according to the manufacturer's instructions, added to the tubes that included each sample and incubated with rotation for 4 h at 4 °C. Samples were then centrifuged (1,000g, 3 min) and washed with low (L)- and high (H)-salt buffers (L, H, L, H, L), centrifuging between washes. Low-salt buffer comprises 50 mM HEPES pH 7.5, 140 mM NaCl, 1% Triton and 1× protease inhibitors without EDTA, and high-salt buffer contains 50 mM HEPES pH 7.5, 500 mM NaCl, 1% Triton and 1× protease inhibitors without EDTA. A final wash was carried out with TE buffer (10 mM Tris-HCl pH 8.0, 1 mM EDTA). Immunoprecipitated chromatin was eluted in elution buffer (1% SDS and 100 mM NaHCO<sub>3</sub>, freshly prepared) by incubation of samples in the buffer for 30 min at 65 °C with agitation. Samples were then centrifuged (1,000g, 3 min), 5 M NaCl was added to a final concentration of 200 mM per sample followed by incubation for between 5 h and overnight at 65 °C, with agitation. Next, Tris-HCl pH 6.8 was added to a final concentration of 40 mM, EDTA to 10 mM, protease K to 50 µg ml<sup>-1</sup> and incubation for 1 h at 45 °C. This product was purified with PCR columns.

**ChIP-seq library construction and sequencing.** Libraries were prepared using the NEBNext Ultra DNA Library Prep for Illumina kit (no. E7370) according to the manufacturer's protocol. Briefly, input and ChIP-enriched DNA were subjected to end repair and the addition of 'A' bases to 3' ends, ligation of the NEB adapter and USER excision. All purification steps were performed using AgenCourt AMPure XP beads (no. A63882, Beckman Coulter). Library amplification was performed by PCR using NEBNext Multiplex Oligos for Illumina (96 Unique Dual Index Primer Pairs, nos. E6440, E6442, E6444, E6446). Final libraries were analyzed using either an Agilent Bioanalyzer or Fragment analyzer High Sensitivity assay (no. 5067-4626 or DNF-474) to estimate the quantity and check size distribution, and were then quantified by quantitative PCR using the KAPA Library Quantification Kit

(no. KK4835, KapaBiosystems). Libraries were sequenced 1 × 50 + 8 + 8 base pairs (bp) on Illumina's NextSeq2000. Between 35 and 40 million reads were obtained per sample.

**ChIP-seq analysis.** Reads were trimmed, adapters removed and low-quality reads discarded using Trimmomatic<sup>76</sup> (v.0.36, TRAILING:5 SLIDINGWINDOW:4:15 MINLEN:36). Reads were then aligned to the mm10 genome with the Burrows–Wheeler aligner<sup>77</sup> (v.0.7.12, -n 2 -l 20 -k 1 -t 2). Each sample was processed individually and, once reads were aligned, the .bam files were merged and deduplicated with SAMtools<sup>78</sup> (v.1.5) and downsampled to 100 million reads to obtain a pool of four replicates per condition. Peaks were called in these pooled files using MACS2 with the parameters -q 0.01 -nomodel -extsize 300 -B -SPMR. Peaks were then annotated to the closest gene with Homer<sup>79</sup> (v.4.11), with those peaks annotated to nonprotein-coding genes not used for further analysis.

### H&E staining

Formalin-fixed, paraffin-embedded (FFPE) blocks were cut into 2–4-µm sections and H&E staining was performed according to the standard protocol.

### Immunofluorescence

In all cases, FFPE blocks were cut into 2–4-µm sections.

IL-17A: following heat-mediated antigen retrieval (20 min at 97 °C with citrate pH 6.0), sections were blocked with 10% goat serum in PBS for 1 h at room temperature. Primary antibody incubation (anti-IL-17A, no. ab79056, abcam 1:200 in EnVision FLEX antibody diluent, Dako) was performed overnight at 4 °C. After three washes in PBS, incubation of secondary antibody (anti-rabbit Alexa Fluor 488, no. A-21206, Molecular Probes, 1:400 in EnVision FLEX antibody diluent, Dako) was carried out at room temperature for 1 h. Nuclei were counterstained with DAPI (5 µg ml<sup>-1</sup> for 10 min at room temperature). Six adult and five aged mice per condition were analyzed.

CD4: antigen retrieval was performed using BOND Epitope Retrieval 2 (no. AR9640, Leica). For primary antibody incubation, rat IgG2b kappa anti-CD4 (clone 4SM95, no. 14-976-682, Thermo Fisher) was used at 1:100 and incubated for 120 min using Leica BOND RX. Nonspecific unions were blocked using 5% goat normal serum mixed with 2.5% bovine serum albumin diluted in wash buffer for 60 min at room temperature. For secondary antibody incubation, goat anti-rat IgG (H + L) and Alexa Fluor 647 (no. A-21247, Thermo Fisher) were used at 1:500 for 60 min. Nuclei were stained with DAPI and slides mounted with fluorescence Mounting Medium (no. S3023, Dako – Agilent). Five adult and five aged mice per condition were analyzed.

### FISH

For *IL17A* and *IL17F*, human adult (22–29 years old, *n* = 4, two women and two men) and aged (60–72 years old, *n* = 4, two women and two men) skin FFPE 5-µm tissue sections were purchased from Genoskin. These samples were approved by the French Ethics Committee and the French Ministry of Research and Higher Education (approval reference no. AC-2022-4863). They were then stained with RNAscope Probes–Hs-IL17A, Interleukin 17A probe (no. 310931, Bio-technique) and Hs-IL17F, Interleukin 17F probe (no. 313901, Bio-technique)—using RNAscope Intro Pack 2.5 HD Reagent Kit Red (no. 322350, Bio-technique). DAPI was used for staining of all nuclei.

For *Rspo3*, FFPE 3-µm tissue sections of mouse back skin from aged/anti-IL-17-treated or aged/IgG control mice were stained with RNAscope Probe Mm-Rspo3-01 (no. 429861, Bio-technique) using RNAscope Intro Pack 2.5 HD Reagent Kit Red (no. 322350, Bio-technique). DAPI was used to stain all nuclei.

### Histopathological analysis

Full images were acquired with a NanoZoomer-2.0 HT C9600 digital scanner (Hamamatsu) with the ×20 objective, in which one pixel

corresponds to 0.46  $\mu\text{m}$ , and coupled to a mercury lamp unit L11600-05 and using NDP.scan 3.4 software U10074-03 (Hamamatsu).

Scaled images were analyzed with Qupath (v.0.3.0 and v.0.3.2). For cornified layer thickness we performed ten measurements per mouse, which were then averaged. Eight mice per condition and age were used. We always ensured that the area analyzed was in the resting hair follicle stage (telogen), to avoid interference of this parameter with the desired quantification. For wound-healing assay, qualitative analysis of dermal granulation tissue and epidermal maturation were performed in a double-blind study by histopathologists. For anagen stage assessment we assigned each hair follicle to an anagen stage based on previous reports<sup>55</sup>.

For immunostaining, multiple selections of the region of interest of the skin dermis, excluding the epidermis and hair follicles, were done manually in two portions of skin. The 'positive cell count' algorithm was used to detect positive cells. Results are presented as the percentage of positive cells. For IL-17A, NDP view2 (v.2.9.29, Hamamatsu) was used to generate snapshots from representative areas. Brightness and contrast were adjusted to help distinguish positive cells from background, using the same parameters for both conditions. For CD4 immunofluorescence, the images displayed in the manuscript were captured with an SP5 confocal microscope (Leica). Images of whole stacks were projected on a single image and brightness and contrast were adjusted to enhance the signal of positive cells, using the same parameters for both conditions. For all immunostaining, these modified images were used exclusively for visualization and never for quantification.

For *IL17A* and *IL17F* FISH, skin upper dermis—excluding the epidermis, hair follicles and skin appendages—was selected manually. In case of tissue artifacts, these were excluded from the region of interest (for example, broken areas, folds). The positive cell count algorithm was used to detect positive labeling in the TRITC channel. Results are presented as the percentage of cells with *IL17A* or *IL17F* signal (either spots—single mRNA copy—or clusters—accumulation of several mRNA copies). For visualization purposes only, representative snapshots were obtained with NDP view2 (v.2.9.29m, Hamamatsu) and brightness and contrast were adjusted to help distinguish FISH signal from background, using the same parameters for both conditions.

For *Rspo3* FISH, dermal papillae were selected manually in well-oriented telogen hair follicles. The 'Cell detection' algorithm was used to detect nuclei within the selected areas, and the 'Subcellular spot detection' algorithm to detect *Rspo3*-positive labeling in the TRITC channel in those nuclei. Individual nuclei were not always distinguishable due to high packing of dermal papillae cells. Therefore, FISH signal (spots and clusters) was not calculated per cell, but per dermal papillae. Five mice per condition were used. Graphical representations were performed with GraphPad Prism 9. For visualization purposes only, representative snapshots were obtained with NDP view2 (v.2.9.29, Hamamatsu) and brightness and contrast were adjusted to help distinguish FISH signal from background, using the same parameters for both conditions. All FISH quantifications were performed on the raw images and never on adjusted ones. Modified images were used exclusively for clearer visualization in figures.

### Bulk RNA-seq library construction and sequencing

For the adult versus aged comparison, libraries were prepared using the TruSeq Stranded Total RNA Library Prep Kit with the Ribo-Zero Human/Mouse/Rat Kit (no. RS-122-2201/2202, Illumina) according to the manufacturer's protocol, using 150–300 ng of total RNA; for ribosomal RNA depletion, RNA was then fragmented for 4.5 min at 94 °C. The remaining steps were followed according to the manufacturer's instructions. Final libraries were analyzed on an Agilent Technologies 2100 Bioanalyzer system using the Agilent DNA 1000 chip to estimate the quantity and validate size distribution; libraries were then quantified by quantitative R using KAPA Library Quantification Kit KK4835

(no. 07960204001, Roche) before amplification with Illumina's cBot. Finally, libraries were sequenced on the Illumina HiSeq 2500 sequencing system using paired-end 50-bp-long reads.

For IL-17-neutralized versus control samples, libraries were prepared using TruSeq stranded mRNA Library Prep (no. 20020595, Illumina) according to the manufacturer's protocol, to convert total RNA to a library of template molecules of known strand origin suitable for subsequent cluster generation and DNA sequencing. Briefly, 500–1,000 ng of total RNA was used for poly(A)-mRNA selection with poly-T oligonucleotides attached to magnetic beads, and two rounds of purification. During the second elution of poly-A RNA, RNA was fragmented under an elevated temperature and primed with random hexamers for complementary DNA synthesis. Cleaved RNA fragments were then copied into first-strand cDNA using reverse transcriptase (SuperScript II, no. 18064-014, Invitrogen) and random primers. Note that the addition of actinomycin D to the First Strand Synthesis Act D mix (FSA) improved strand specificity by prevention of spurious DNA-dependent synthesis while allowing RNA-dependent synthesis. Second-strand cDNA was then synthesized by removal of the RNA template and synthesis of a replacement strand, incorporating dUTP in place of dTTP to generate double-stranded cDNA using DNA polymerase I and RNase H. These cDNA fragments then had a single A base added to the 3' ends of the blunt fragments, to prevent them from ligating to one another during adapter ligation. A corresponding single T-nucleotide on the 3' end of the adapter provided a complementary overhang for ligation of the adapter to the fragments, ensuring a low rate of chimera (concatenated template) formation. Subsequent ligation of the multiple indexing adapter to the ends of ds-cDNA was carried out. Finally, PCR selectively enriched DNA fragments with adapter molecules on both ends, and the amount of DNA in the library was amplified. PCR was performed with a PCR Primer Cocktail that anneals to the ends of the adapters. Final libraries were analyzed using either Bioanalyzer DNA 1000 or Fragment Analyzer Standard Sensitivity (Agilent) to estimate the quantity and validate size distribution; libraries were then quantified by quantitative PCR using KAPA Library Quantification Kit KK4835 (Roche) before amplification with Illumina's cBot. Finally, libraries were sequenced on the Illumina HiSeq 2500 sequencing system using single-end 50-bp-long reads.

### 10X scRNA-seq

Stained dermal single-cell suspensions were prepared as described above. CD45<sup>+</sup> and CD45<sup>+</sup>EpCAM<sup>-</sup> cells were FACS sorted separately in a BD Fusion cell sorter to enrich for the less abundant CD45<sup>+</sup> cells following the sorting strategy shown in Supplementary Fig. 1a. Cells were collected in PBS + 0.5% bovine serum albumin at 4 °C in LoBind tubes (Eppendorf) and processed immediately with the microfluidics Chromium platform (10X Genomics). For the adult and aged experiment, three technical replicates were performed for CD45<sup>+</sup> sorting. Replicate 1 included skin dermal cells of three adult and one aged mice, replicate 2 had two adult and one aged mice and replicate 3 comprised two adult and two aged mice. For CD45<sup>+</sup>EpCAM<sup>-</sup> cell sorting two replicates were carried out, both comprising one mouse per condition. For aged/IL-17-blocked and aged/IgG control 10X scRNA-seq of dermal skin cells, both CD45<sup>+</sup> and CD45<sup>+</sup>EpCAM<sup>-</sup> conditions included four replicates in total. In both conditions, replicate 1 consisted of two aged/IL-17-blocked and two aged/IgG control mice. Replicates 2, 3 and 4 consisted in all cases of one aged/IL-17-blocked and one aged/IgG control mouse.

### Data preprocessing

Sequences were demultiplexed and aligned according to the Cell Ranger pipeline (v.6.0.0) with default parameters. Sequencing reads were mapped against the mouse GRCm38 reference genome to generate feature-barcode matrices separately for all CD45<sup>+</sup> and CD45<sup>+</sup> replicates.

### Quality control and technical bias corrections

Gene count matrixes were analyzed with the Seurat package (v.4.0.4) in R (v.4.0.3)<sup>80</sup>. Replicates were merged, analyzed and annotated separately for CD45<sup>+</sup> and CD45<sup>-</sup> datasets before integration. Cells were filtered with >10% of mitochondrial gene content and genes not found in at least five cells. As part of quality control, cells situated between the minimum and first quartile (according to the distribution of number of genes per cell of each compartment dataset) were removed. To avoid contamination of epithelial cells in the immune compartment, EPCAM<sup>+</sup> cells found in CD45<sup>+</sup> sorted cells were filtered out.

In addition, to remove technical bias arising after merging the different replicates we computed differentially expressed genes among replicates using the function FindAllMarkers, then we ensured that the top 500 differentially expressed genes between replicates were not present in highly variable genes (HVGs). Thus we removed the intersection between computed differentially expressed genes and HVG.

To evaluate integration of the different replicates we used the local inverse Simpson's index (LISI) (<https://github.com/immunogenomics/LISI>)<sup>30</sup>. This score defines the effective number of samples in the local neighborhood of a cell. Under ideal mixing we would expect to obtain LISI scores equal to the number of different replicates in our datasets. This indicates that the neighborhoods are well represented by all samples and that the cell types/states previously identified exhibit good mixing across all replicates. In addition we assessed the performance of replicate integration by qualitative inspection of UMAPs. We checked that all cell types and states were well represented by each replicate and that our dataset did not contain any technical cluster entirely driven by replicate effect.

### Clustering

Cell-to-cell variations were normalized by expression values using a scale factor of 100,000 and log transformation. Gene expression measurements were scaled and centered. Scaled z-score values were then used as normalized gene measurement input for both clustering and visualization of differences in expression between cell clusters. HVGs were selected by assessment of the relationship of log(variance) and log(mean) and choosing those with the highest variance:mean ratio. Principal component analysis was used to reduce the dimensionality of the dataset, and ElbowGraph to select the number of dimensions for the clustering of significant principal components. Cluster identification was performed using the functions FindNeighbors and FindClusters, which calculate *k*-nearest neighbors and generate the shared nearest-neighbor graph to cluster cells. The algorithm applied was the Louvain method, which allows tuning of the number of clusters with a resolution parameter. To explore clusters in more detail, either the resolution parameter was increased in FindClusters function or FindSubCluster was used for specific clusters. UMAP was used as a nondimensional reduction method to visualize clustering.

In the case of the aged/control IgG-treated versus aged/anti-IL-17A/F-treated fibroblast clusters, we conducted a subclustering analysis of all populations obtained to detect potential fibroblast populations responding to the blocking treatment. With this we separated the previously named fibroblast 1 cluster obtained in the aged versus adult comparison into three subclusters (fibroblasts 1.0–1.2). Then, fibroblast 2 cluster was divided into two new clusters (fibroblasts 2.0 and 2.1) and fibroblast 3 cluster was separated into four clusters (fibroblasts 3.0–3.3); fibroblast 4 and 5 clusters remained as separate units. This separation allowed detection of subtle differences in the IL-17A/F blockade response in fibroblast subgroups.

### Cell type annotation

For annotation of cell types and states, enriched genes were first identified in each of the clusters with the function FindAllMarkers using the Wilcoxon rank-sum test to find cluster-specific markers. These cluster-specific genes were then explored to find previously

reported cell population marker genes. Examples of marker genes used to annotate the cell populations include: CD4<sup>+</sup> T cells: *Cd28* and *Cd4*; CD8<sup>+</sup> T cells: *Cd8a* and *Cd8b1*; dermal cells: *Cd207*; fibroblast 1: *Crabp1*, *Inhba* and *Notum*; fibroblast 2: *Col1a1*, *Col1a2*, *Cd34*, *Robo1* and *Col3a1*; fibroblast 3: *Efemp1*, *Ilir2* and *Ccl11*; fibroblast 4: *Col11a1*, *Aspn* and *Coch*; fibroblast 5: *Myoc* and *Dcn*; ILCs: *Il13* and *Kit*; lymphatic endothelial cells: *Lyve1* and *Hes1*; macrophage 1: *Il1b*; macrophage 2: *Tnfsf9*; macrophage 3: *Ear2* and *Cd163*; monocyte 1: *Plac8* and *Cd14*; monocyte 2: *Ccl8* and *C1qa*; monocyte 3: *Retnla*, *C1qb* and *Ccr2*; natural killer cells: *Gzmc*, *Ccl5* and *Nkg7*; pericytes: *Acta2* and *Rgs5*; proliferating macrophages: *Mki67*; proliferating T cells: *Hmgb2*; Schwann cells: *Cryab*, *Plekha4* and *Scn7a*; Schwann cells 1: *Kcna1*; Schwann cells 2: *Sox10*; T regulatory cells: *Foxp3*; venous endothelial cell arterioles and capillaries: *Ptprb* and *Flt1*; venous endothelial cell venules: *Aqp1*, *Sele* and *Pecam1*; and  $\gamma\delta$  T cells: *Trdc* and *Trgc1*. For the annotation of IgG-treated versus anti-IL-17A/F-treated clusters we used the markers mentioned above.

### Differential expression analysis for each cluster

To find differentially expressed genes between adult versus aged, and IgG-treated versus anti-IL-17A/F-treated, in different annotated cell type populations, differential expression analysis was performed between conditions for each cluster with the function FindMarkers. To control for multiple comparisons we used the FDR Benjamini–Hochberg method.

### Age effect analysis

To assess age-related effects among immune cells, a deep learning approach was created based on autoencoders. During training this method can identify features relevant to the data structure and then use them to predict different cell types in a test dataset. To generate the model, adult data were divided into two smaller subsets that could be used as training and test sets. The model displayed high probability scores ( $P > 0.5$ ) in the prediction of cell types from the test set among the different immune cell types and a low rate of unclassified cells (unclassified rate <5%). If the rate of unclassified cell type is strictly biased for aged cells, this would reflect the effect of aging on the cell phenotype. Based on this assumption an age-deviance score was defined as  $1 - q$ , where  $q$  is the probability of the unclassified cell being in the true corresponding cell type class in aged cells. The proportion of unclassified cells within each cell type in aged cells, and the proportion of age-affected cells, were then measured and normalized by the model's error rate (for example, by subtracting the cell proportion in each adult cell type that could not be predicted by the model).

### Cell composition analysis

To evaluate the significance of differences in cell type abundance between conditions we applied sccomp<sup>81</sup>, a tool designed for differential composition and variability analyses that relies on sum-constrained independent beta-binomial distributions. This model uses mean-variability association, which allows modeling of the compositional properties of the data while enabling the exclusion of outliers. We assessed significant differences (FDR < 0.025, using a Benjamini–Hochberg procedure to control for multiple testing) for composition and/or group-specific variability in each cell type population, comparing adult versus aged conditions and aged/anti-IL-17A/F-treated versus aged/IgG-treated control.

### Bioinformatics analyses of bulk RNA-seq data

FastQ files were aligned against the mm10 reference genome using STAR2.5.2b<sup>82</sup> with default options. Unless otherwise specified, all downstream analyses were performed using R 3.5.1. Differentially expressed genes (DEGs) between conditions were determined using DESeq2 1.22.1 (ref. 83), using mm10 gene counts as generated by the function featureCounts from the RSubread package v.1.32.4 (ref. 84), with

options annot.inbuilt = 'mm10', allowMultiOverlap = TRUE, countMulti MappingReads = FALSE, minMQS = 1, ignoreDup = FALSE). Genes were selected as DEGs with the thresholds  $|\log_2(\text{foldChange})| > 1.25$  and Benjamini–Hochberg-determined  $P < 0.1$ , using experimental batch as covariate. Gene set enrichment analysis was performed using gene set collections at the *Mus musculus* gene symbol level. Gene set collections used were GOBP, GOMF, GOCC and KEGG, obtained using the package org.Mm.eg.db (November 2014); GOSLIM, obtained from geneontology.org (November 2014); and Broad Hallmarks, obtained from the Broad Institute MSigDB website (<https://www.gsea-msigdb.org/gsea/msigdb/>) and mapped from human to mouse genes using homology information from Ensembl biomart archive (July 2016). Analyses were performed using regularized log transformation (rlog) applied to count data using the DESeq2 R package 1.22, with ROAST<sup>85</sup> and the MaxMean statistic (<http://statweb.stanford.edu/~tibs/GSA/>).

### GO analysis

GO analysis for scRNA-seq was performed on lists ranked by increasing Benjamini–Hochberg-adjusted  $P$  values with g:Profiler<sup>86</sup> (<https://biit.cs.ut.ee/gprofiler/gost>), using the biological processes database. A GO category was considered significant with adjusted  $P < 0.05$ . In the aged versus adult comparison, genes with fold change  $> 0.35$  ( $\log_2$ ) were considered. In the aged/anti-IL-17A/F-treated versus aged/IgG-treated control, genes with fold change  $> 0.25$  ( $\log_2$ ) were considered.

GO analysis for both epidermal bulk RNA-seq and p65 ChIP-seq was performed with enrichR<sup>87</sup> (<https://maayanlab.cloud/Enrichr/>). A category was considered significant when  $P < 0.01$ .

### Statistics and reproducibility

No statistical methods were used to predetermine sample size. This was decided taking into the account variability between samples, particularly in aged mice, and was based on our expertise with the skin of aged mice<sup>1,2,22</sup>.

In general graphs show individual values and median (depicted as a line) and  $P$  values were obtained using the nonparametric two-tailed Mann–Whitney  $U$ -test with Prism v.9, unless otherwise stated in the figure legends.

Data collection and analysis were not performed blind to the conditions of the experiments, except for the histopathological wound healing analysis.

### Reporting summary

Further information on research design is available in the Nature Portfolio Reporting Summary linked to this article.

### Data availability

RNA-seq data are deposited at the NCBI GEO repository with accessions GSE190182 (<https://www.ncbi.nlm.nih.gov/geo/query/acc.cgi?acc=GSE190182>) and GSE190393 (<https://www.ncbi.nlm.nih.gov/geo/query/acc.cgi?acc=GSE190393>) for epidermal bulk RNA-seq data, and GSE193920 (<https://www.ncbi.nlm.nih.gov/geo/query/acc.cgi?acc=GSE193920>) for scRNA-seq data. ChIP-seq data are deposited at the NCBI GEO repository with accession GSE213732 (<https://www.ncbi.nlm.nih.gov/geo/query/acc.cgi?acc=GSE213732>). scRNA-seq analysis scripts are available at <https://github.com/mereulab/IL17-SkinAging>. The remaining data generated or analyzed during this study are included in this published article (and its Supplementary Information files). GO biological processes categories can be found at g:Profiler<sup>86</sup> (<https://biit.cs.ut.ee/gprofiler/gost>).

### References

- Sato, S. et al. Circadian reprogramming in the liver identifies metabolic pathways of aging. *Cell* **170**, 664–677 (2017).
- Solanas, G. et al. Aged stem cells reprogram their daily rhythmic functions to adapt to stress. *Cell* **170**, 678–692 (2017).
- Lopez-Otin, C., Blasco, M. A., Partridge, L., Serrano, M. & Kroemer, G. The hallmarks of aging. *Cell* **153**, 1194–1217 (2013).
- Green, D. R., Galluzzi, L. & Kroemer, G. Mitochondria and the autophagy-inflammation-cell death axis in organismal aging. *Science* **333**, 1109–1112 (2011).
- Dimri, G. P. et al. A biomarker that identifies senescent human cells in culture and in aging skin in vivo. *Proc. Natl Acad. Sci. USA* **92**, 9363–9367 (1995).
- Salvioli, S. et al. Immune system, cell senescence, aging and longevity–inflamm-aging reappraised. *Curr. Pharm. Des.* **19**, 1675–1679 (2013).
- Solanas, G. & Benitah, S. A. Regenerating the skin: a task for the heterogeneous stem cell pool and surrounding niche. *Nat. Rev. Mol. Cell Biol.* **14**, 737–748 (2013).
- Ghadially, R., Brown, B. E., Sequeira-Martin, S. M., Feingold, K. R. & Elias, P. M. The aged epidermal permeability barrier. Structural, functional, and lipid biochemical abnormalities in humans and a senescent murine model. *J. Clin. Invest.* **95**, 2281–2290 (1995).
- Giangreco, A., Qin, M., Pintar, J. E. & Watt, F. M. Epidermal stem cells are retained in vivo throughout skin aging. *Aging Cell* **7**, 250–259 (2008).
- Doles, J., Storer, M., Cozzuto, L., Roma, G. & Keyes, W. M. Age-associated inflammation inhibits epidermal stem cell function. *Genes Dev.* **26**, 2144–2153 (2012).
- Benitah, S. A. & Welz, P. S. Circadian regulation of adult stem cell homeostasis and aging. *Cell Stem Cell* **26**, 817–831 (2020).
- Choi, E. H. Aging of the skin barrier. *Clin. Dermatol.* **37**, 336–345 (2019).
- Ge, Y. et al. The aging skin microenvironment dictates stem cell behavior. *Proc. Natl Acad. Sci. USA* **117**, 5339–5350 (2020).
- Liu, N. et al. Stem cell competition orchestrates skin homeostasis and ageing. *Nature* **568**, 344–350 (2019).
- Matsumura, H. et al. Hair follicle aging is driven by transepidermal elimination of stem cells via COL17A1 proteolysis. *Science* **351**, aad4395 (2016).
- Giangreco, A., Goldie, S. J., Failla, V., Saintigny, G. & Watt, F. M. Human skin aging is associated with reduced expression of the stem cell markers beta1 integrin and MCSP. *J. Invest. Dermatol.* **130**, 604–608 (2010).
- Koester, J. et al. Niche stiffening compromises hair follicle stem cell potential during ageing by reducing bivalent promoter accessibility. *Nat. Cell Biol.* **23**, 771–781 (2021).
- Mahmoudi, S. et al. Heterogeneity in old fibroblasts is linked to variability in reprogramming and wound healing. *Nature* **574**, 553–558 (2019).
- Gould, L. et al. Chronic wound repair and healing in older adults: current status and future research. *J. Am. Geriatr. Soc.* **63**, 427–438 (2015).
- Norman, R. A. Geriatric dermatology. *Dermatol. Ther.* **16**, 260–268 (2003).
- Jin, S. P. et al. Changes in tight junction protein expression in intrinsic aging and photoaging in human skin in vivo. *J. Dermatol. Sci.* **84**, 99–101 (2016).
- Salzer, M. C. et al. Identity noise and adipogenic traits characterize dermal fibroblast aging. *Cell* **175**, 1575–1590 (2018).
- Sole-Boldo, L. et al. Single-cell transcriptomes of the human skin reveal age-related loss of fibroblast priming. *Commun. Biol.* **3**, 188 (2020).
- Joost, S. et al. The molecular anatomy of mouse skin during hair growth and rest. *Cell Stem Cell* **26**, 441–457 (2020).
- Reynolds, G. et al. Developmental cell programs are co-opted in inflammatory skin disease. *Science* <https://doi.org/10.1126/science.aba6500> (2021).
- Tabula Muris, C. A single-cell transcriptomic atlas characterizes ageing tissues in the mouse. *Nature* **583**, 590–595 (2020).

27. Keyes, B. E. et al. Impaired epidermal to dendritic T cell signaling slows wound repair in aged skin. *Cell* **167**, 1323–1338 (2016).
28. Ali, N. et al. Regulatory T cells in skin facilitate epithelial stem cell differentiation. *Cell* **169**, 1119–1129 (2017).
29. Bhushan, M. et al. Tumour necrosis factor- $\alpha$ -induced migration of human Langerhans cells: the influence of ageing. *Br. J. Dermatol.* **146**, 32–40 (2002).
30. Korsunsky, I. et al. Fast, sensitive and accurate integration of single-cell data with Harmony. *Nat. Methods* **16**, 1289–1296 (2019).
31. Stuart, T. et al. Comprehensive integration of single-cell data. *Cell* **177**, 1888–1902 (2019).
32. Zou, Z. et al. A single-cell transcriptomic atlas of human skin aging. *Dev. Cell* **56**, 383–397 (2021).
33. Muhl, L. et al. Single-cell analysis uncovers fibroblast heterogeneity and criteria for fibroblast and mural cell identification and discrimination. *Nat. Commun.* **11**, 3953 (2020).
34. Driskell, R. R. et al. Distinct fibroblast lineages determine dermal architecture in skin development and repair. *Nature* **504**, 277–281 (2013).
35. Rendl, M., Polak, L. & Fuchs, E. BMP signaling in dermal papilla cells is required for their hair follicle-inductive properties. *Genes Dev.* **22**, 543–557 (2008).
36. Frisch, S. M. & MacFawn, I. P. Type I interferons and related pathways in cell senescence. *Aging Cell* **19**, e13234 (2020).
37. Waldera Lupa, D. M. et al. Characterization of skin aging-associated secreted proteins (SAASP) produced by dermal fibroblasts isolated from intrinsically aged human skin. *J. Invest. Dermatol.* **135**, 1954–1968 (2015).
38. Pasparakis, M., Haase, I. & Nestle, F. O. Mechanisms regulating skin immunity and inflammation. *Nat. Rev. Immunol.* **14**, 289–301 (2014).
39. Eming, S. A., Martin, P. & Tomic-Canic, M. Wound repair and regeneration: mechanisms, signaling, and translation. *Sci. Transl. Med.* **6**, 265sr266 (2014).
40. Li, X., Bechara, R., Zhao, J., McGeachy, M. J. & Gaffen, S. L. IL-17 receptor-based signaling and implications for disease. *Nat. Immunol.* **20**, 1594–1602 (2019).
41. Chakievska, L. et al. IL-17A is functionally relevant and a potential therapeutic target in bullous pemphigoid. *J. Autoimmun.* **96**, 104–112 (2019).
42. Blauvelt, A. & Chiricozzi, A. The immunologic role of IL-17 in psoriasis and psoriatic arthritis pathogenesis. *Clin. Rev. Allergy Immunol.* **55**, 379–390 (2018).
43. Liu, T. et al. The IL-23/IL-17 pathway in inflammatory skin diseases: from bench to bedside. *Front. Immunol.* **11**, 594735 (2020).
44. Warren, R. B. et al. Bimekizumab versus adalimumab in plaque psoriasis. *N. Engl. J. Med.* **385**, 130–141 (2021).
45. Chen, H. C. et al. IL-7-dependent compositional changes within the gammadelta T cell pool in lymph nodes during ageing lead to an unbalanced anti-tumour response. *EMBO Rep.* **20**, e47379 (2019).
46. Ouyang, X. et al. Potentiation of Th17 cytokines in aging process contributes to the development of colitis. *Cell Immunol.* **266**, 208–217 (2011).
47. Bharath, L. P. et al. Metformin enhances autophagy and normalizes mitochondrial function to alleviate aging-associated inflammation. *Cell Metab.* **32**, 44–55 (2020).
48. Ciofani, M. et al. A validated regulatory network for Th17 cell specification. *Cell* **151**, 289–303 (2012).
49. Yamazaki, T. et al. CCR6 regulates the migration of inflammatory and regulatory T cells. *J. Immunol.* **181**, 8391–8401 (2008).
50. Carr, T. M., Wheaton, J. D., Houtz, G. M. & Ciofani, M. JunB promotes Th17 cell identity and restrains alternative CD4<sup>(+)</sup> T-cell programs during inflammation. *Nat. Commun.* **8**, 301 (2017).
51. Kobayashi, T., Ricardo-Gonzalez, R. R. & Moro, K. Skin-resident innate lymphoid cells – cutaneous innate guardians and regulators. *Trends Immunol.* **41**, 100–112 (2020).
52. Drujont, L. et al. ROR $\gamma$ mat<sup>+</sup> cells selectively express redundant cation channels linked to the Golgi apparatus. *Sci. Rep.* **6**, 23682 (2016).
53. McGinley, A. M. et al. Interleukin-17A serves a priming role in autoimmunity by recruiting IL-1 $\beta$ -producing myeloid cells that promote pathogenic T cells. *Immunity* **52**, 342–356 (2020).
54. Ito, M. et al. Wnt-dependent de novo hair follicle regeneration in adult mouse skin after wounding. *Nature* **447**, 316–320 (2007).
55. Muller-Rover, S. et al. A comprehensive guide for the accurate classification of murine hair follicles in distinct hair cycle stages. *J. Invest. Dermatol.* **117**, 3–15 (2001).
56. Ghadially, R. et al. Decreased epidermal lipid synthesis accounts for altered barrier function in aged mice. *J. Invest. Dermatol.* **106**, 1064–1069 (1996).
57. Pastar, I. et al. Epithelialization in wound healing: a comprehensive review. *Adv. Wound Care (New Rochelle)* **3**, 445–464 (2014).
58. Hsu, Y. C., Li, L. & Fuchs, E. Emerging interactions between skin stem cells and their niches. *Nat. Med.* **20**, 847–856 (2014).
59. Stojadinovic, O. et al. Molecular pathogenesis of chronic wounds: the role of beta-catenin and c-myc in the inhibition of epithelialization and wound healing. *Am. J. Pathol.* **167**, 59–69 (2005).
60. Singer, A. J. & Clark, R. A. Cutaneous wound healing. *N. Engl. J. Med.* **341**, 738–746 (1999).
61. Singh, T. P. et al. Involvement of IL-9 in Th17-associated inflammation and angiogenesis of psoriasis. *PLoS ONE* **8**, e51752 (2013).
62. Markovic, I. & Savvides, S. N. Modulation of signaling mediated by TSLP and IL-7 in inflammation, autoimmune diseases, and cancer. *Front. Immunol.* **11**, 1557 (2020).
63. Sevilla, L. M. et al. Mice deficient in involucrin, envoplakin, and periplakin have a defective epidermal barrier. *J. Cell Biol.* **179**, 1599–1612 (2007).
64. Coulombe, P. A., Kopan, R. & Fuchs, E. Expression of keratin K14 in the epidermis and hair follicle: insights into complex programs of differentiation. *J. Cell Biol.* **109**, 2295–2312 (1989).
65. Estrach, S., Cordes, R., Hozumi, K., Gossler, A. & Watt, F. M. Role of the Notch ligand Delta1 in embryonic and adult mouse epidermis. *J. Invest. Dermatol.* **128**, 825–832 (2008).
66. Pentimikko, N. et al. Notum produced by Paneth cells attenuates regeneration of aged intestinal epithelium. *Nature* **571**, 398–402 (2019).
67. Brack, A. S. et al. Increased Wnt signaling during aging alters muscle stem cell fate and increases fibrosis. *Science* **317**, 807–810 (2007).
68. Kusumbe, A. P. et al. Age-dependent modulation of vascular niches for haematopoietic stem cells. *Nature* **532**, 380–384 (2016).
69. Dulken, B. W. et al. Single-cell analysis reveals T cell infiltration in old neurogenic niches. *Nature* **571**, 205–210 (2019).
70. Ambrosi, T. H. et al. Aged skeletal stem cells generate an inflammatory degenerative niche. *Nature* **597**, 256–262 (2021).
71. Kalamakis, G. et al. Quiescence modulates stem cell maintenance and regenerative capacity in the aging brain. *Cell* **176**, 1407–1419 (2019).
72. Yang, D. & de Haan, G. Inflammation and aging of hematopoietic stem cells in their niche. *Cells* <https://doi.org/10.3390/cells10081849> (2021).
73. Miossec, P. Update on interleukin-17: a role in the pathogenesis of inflammatory arthritis and implication for clinical practice. *RMD Open* **3**, e000284 (2017).



74. Konieczny, P. et al. Interleukin-17 governs hypoxic adaptation of injured epithelium. *Science* **377**, eabg9302 (2022).
75. Uberoi, A. et al. Commensal microbiota regulates skin barrier function and repair via signaling through the aryl hydrocarbon receptor. *Cell Host Microbe* **29**, 1235–1248 (2021).
76. Bolger, A. M., Lohse, M. & Usadel, B. Trimmomatic: a flexible trimmer for Illumina sequence data. *Bioinformatics* **30**, 2114–2120 (2014).
77. Li, H. & Durbin, R. Fast and accurate short read alignment with Burrows-Wheeler transform. *Bioinformatics* **25**, 1754–1760 (2009).
78. Danecek, P. et al. Twelve years of SAMtools and BCFtools. *Gigascience* <https://doi.org/10.1093/gigascience/giab008> (2021).
79. Heinz, S. et al. Simple combinations of lineage-determining transcription factors prime cis-regulatory elements required for macrophage and B cell identities. *Mol. Cell* **38**, 576–589 (2010).
80. Hao, Y. et al. Integrated analysis of multimodal single-cell data. *Cell* **184**, 3573–3587 (2021).
81. Mangiola, S. S. et al. Robust differential composition and variability analysis for multisample cell omics. Preprint at *bioRxiv* <https://doi.org/10.1101/2022.03.04.482758> (2022).
82. Dobin, A. et al. STAR: ultrafast universal RNA-seq aligner. *Bioinformatics* **29**, 15–21 (2013).
83. Love, M. I., Huber, W. & Anders, S. Moderated estimation of fold change and dispersion for RNA-seq data with DESeq2. *Genome Biol.* **15**, 550 (2014).
84. Liao, Y., Smyth, G. K. & Shi, W. The R package Rsubread is easier, faster, cheaper and better for alignment and quantification of RNA sequencing reads. *Nucleic Acids Res.* **47**, e47 (2019).
85. Wu, D. et al. ROAST: rotation gene set tests for complex microarray experiments. *Bioinformatics* **26**, 2176–2182 (2010).
86. Raudvere, U. et al. g:Profiler: a web server for functional enrichment analysis and conversions of gene lists (2019 update). *Nucleic Acids Res* **47**, W191–W198 (2019).
87. Xie, Z. et al. Gene set knowledge discovery with Enrichr. *Curr. Protoc.* **1**, e90 (2021).

## Acknowledgements

Research in the S.A.B. laboratory is supported partially by the European Research Council under the European Union's Horizon 2020 research and innovation program (grant agreement no. 787041), the Government of Cataluña (SGR grant), the Government of Spain (MINECO) and Foundation Lilliane Bettencourt. This work was partially supported by a Leonardo grant (BBVA Foundation) awarded to G.S. P.S. was awarded a Spanish Ministry of Economy and Development fellowship (MINECO, no. BES-2017-081279). J.B. was awarded a Spanish Ministry of Science and Innovation fellowship (MCI, no. PRE-2021-097118). M.E. and E.M. were supported by Ministerio de Ciencia e Innovación (MCI), Agencia Estatal de Investigación (AEI) and the European Development Regional Fund, 'A way to make Europe' ERDF (no. RTI2018-094049-B-I00). H.H. has received funding from Ministerio de Ciencia, Innovación y Universidades (no. SAF2017-89109-P; AEI/FEDER, UE). IRB Barcelona is a Severo Ochoa Center of Excellence (MINECO award no. SEV-2015-0505). The funders had no role in study design, data collection and analysis, decision to publish or preparation of the manuscript. We thank the histopathology,

advanced digital microscopy and genomics facilities of IRB Barcelona and the genomics unit at CRG. We thank C. Niessen and E. Wachsmuth for useful tips on TEWL usage. We thank V. Raker for manuscript editing.

## Author contributions

P.S., J.B. and G.S. designed the experiments and collected, analyzed and interpreted data. E.M. and M.C.-P. analyzed and interpreted scRNA-seq data. N.P. and M.A. performed histopathological analyses of part of the histological techniques. O.R. and E.B. performed RNA-seq bioinformatics analysis. M.E., H.H. and L.D.C. financially supported the project and helped with data interpretation. G.S., S.A.B. and H.H. conceived and supervised the project and drafted the article. All authors contributed to the final manuscript.

## Competing interests

The authors declare no competing interests.

## Additional information

**Extended data** is available for this paper at <https://doi.org/10.1038/s43587-023-00431-z>.

**Supplementary information** The online version contains supplementary material available at <https://doi.org/10.1038/s43587-023-00431-z>.

**Correspondence and requests for materials** should be addressed to Holger Heyn, Guiomar Solanas or Salvador Aznar Benitah.

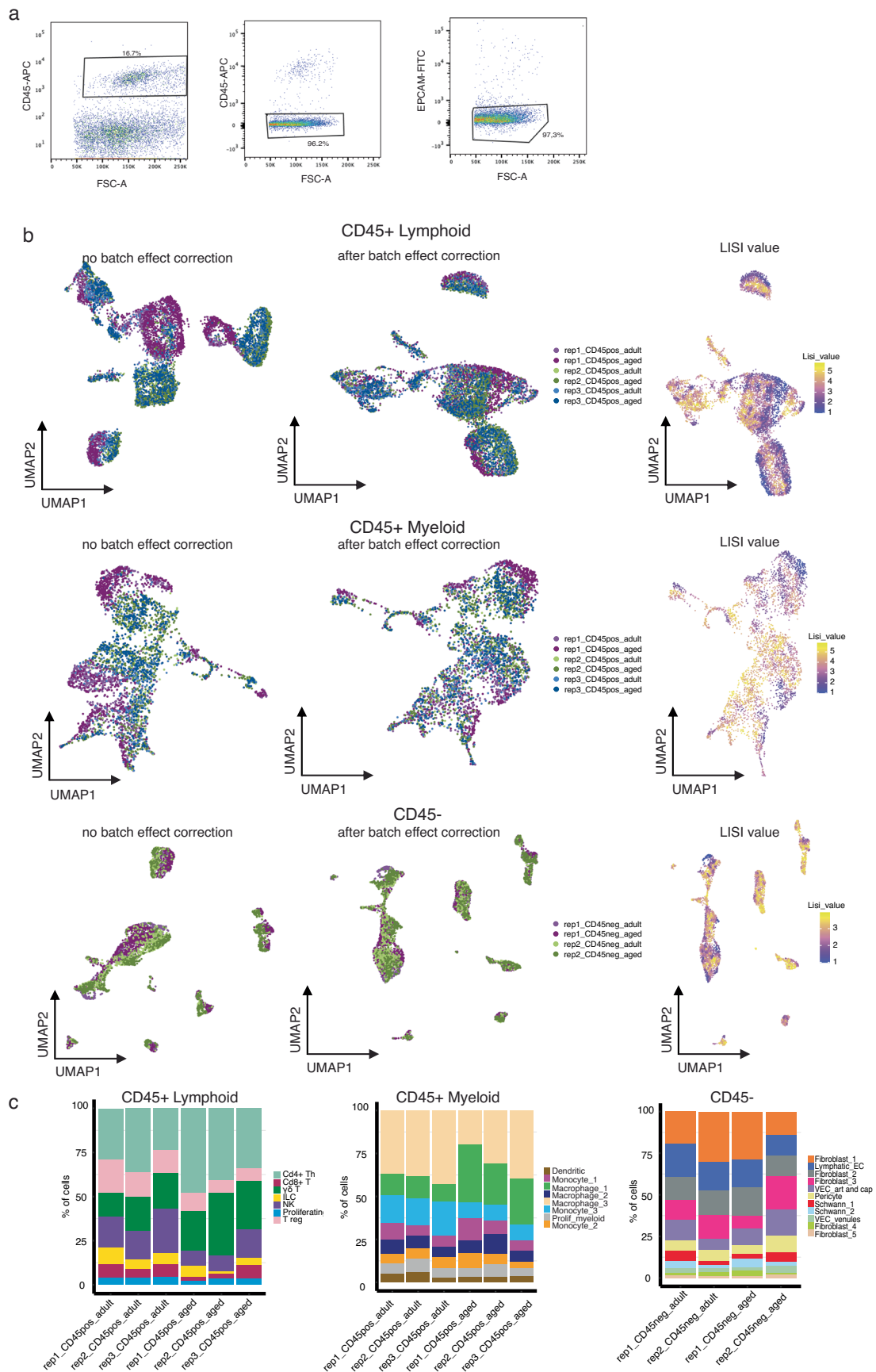
**Peer review information** *Nature Aging* thanks Maria Kasper, Emi Nishimura and the other, anonymous, reviewer(s) for their contribution to the peer review of this work.

**Reprints and permissions information** is available at [www.nature.com/reprints](http://www.nature.com/reprints).

**Publisher's note** Springer Nature remains neutral with regard to jurisdictional claims in published maps and institutional affiliations.

**Open Access** This article is licensed under a Creative Commons Attribution 4.0 International License, which permits use, sharing, adaptation, distribution and reproduction in any medium or format, as long as you give appropriate credit to the original author(s) and the source, provide a link to the Creative Commons license, and indicate if changes were made. The images or other third party material in this article are included in the article's Creative Commons license, unless indicated otherwise in a credit line to the material. If material is not included in the article's Creative Commons license and your intended use is not permitted by statutory regulation or exceeds the permitted use, you will need to obtain permission directly from the copyright holder. To view a copy of this license, visit <http://creativecommons.org/licenses/by/4.0/>.

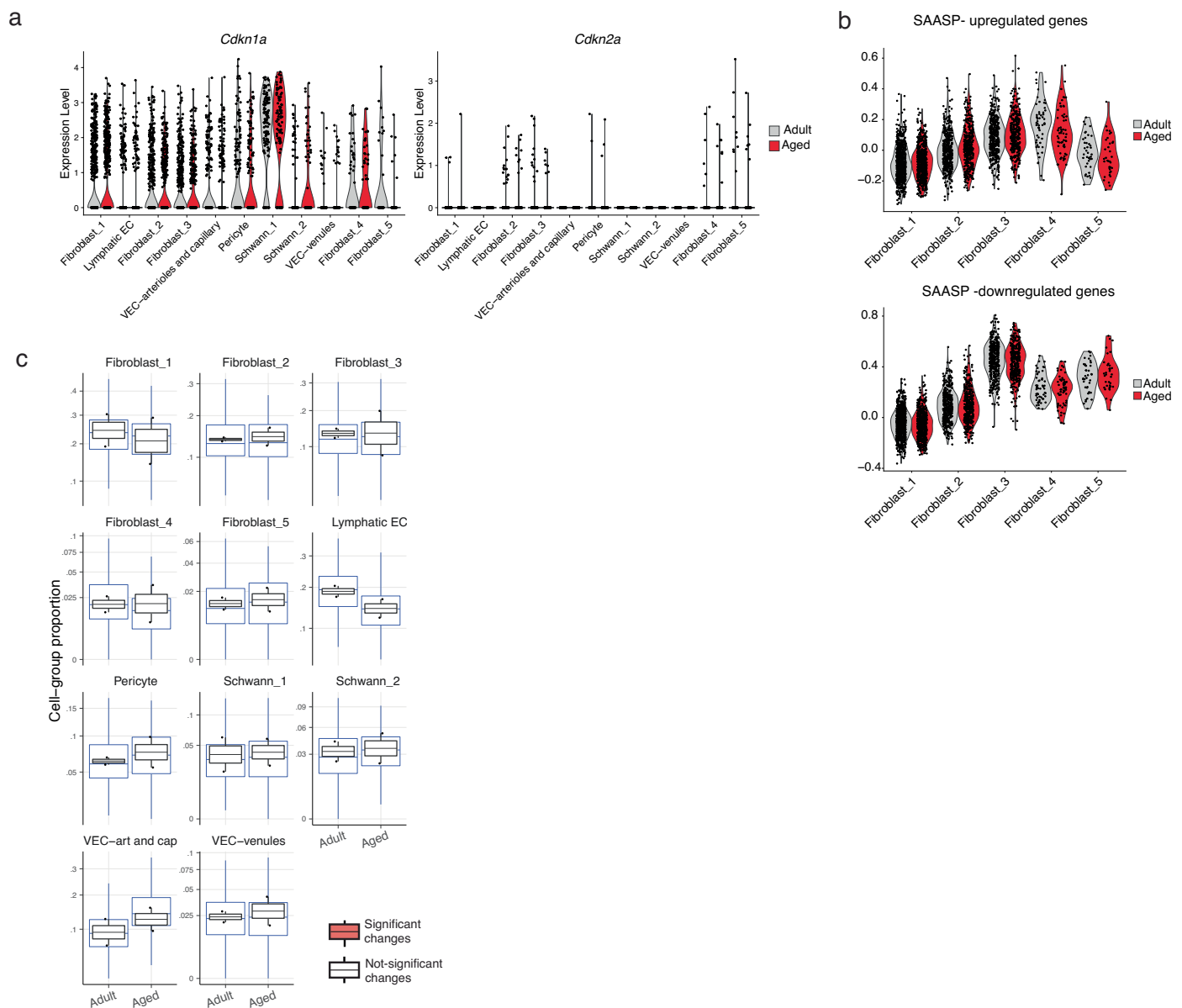
© The Author(s) 2023



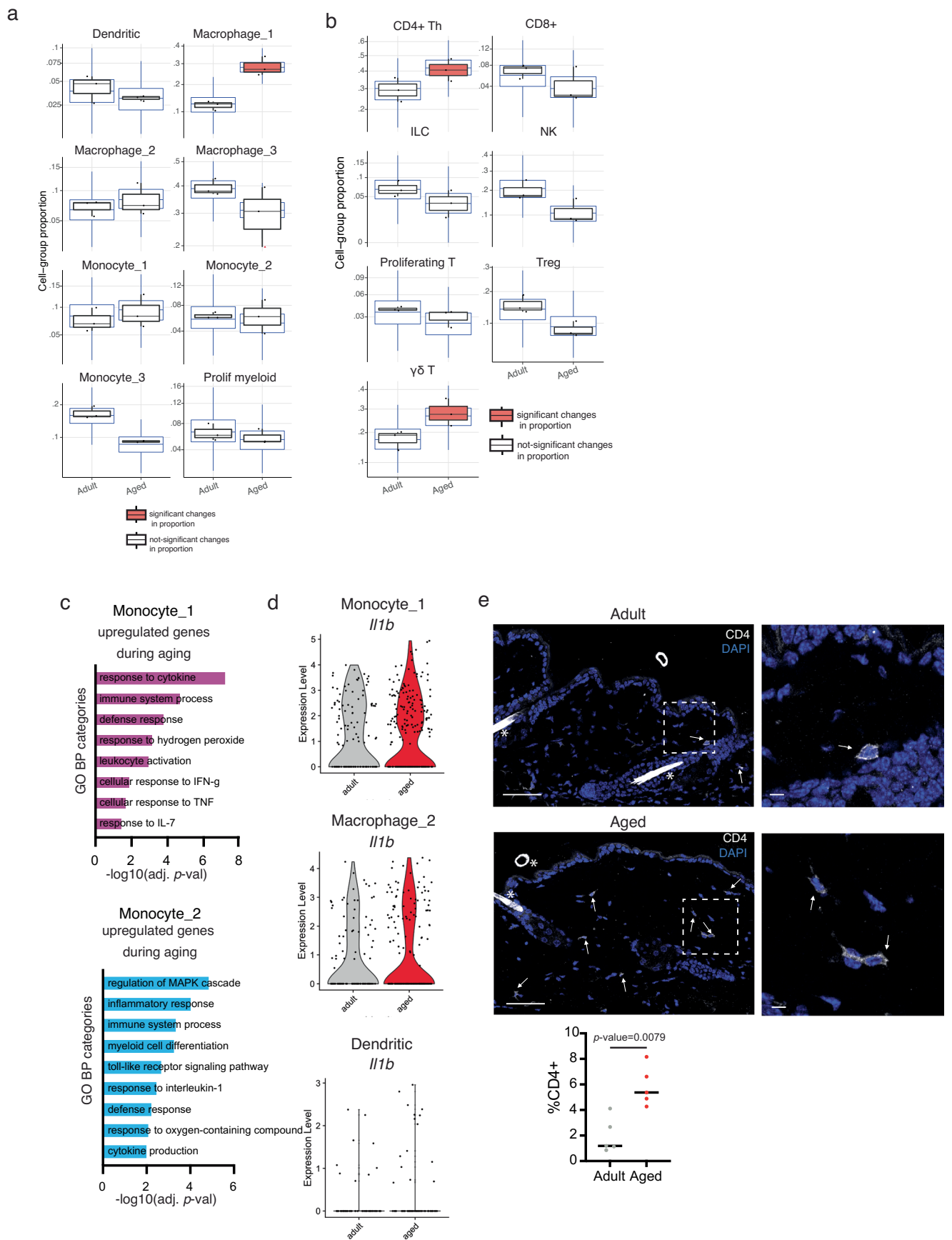
Extended Data Fig. 1 | See next page for caption.

**Extended Data Fig. 1 | Sorting strategy and quality controls of scRNA-seq of adult and aged dermis.** **a**, Flow cytometry plots representative of the sorting strategy followed to obtain CD45<sup>+</sup> and CD45<sup>-</sup>/EpCAM<sup>-</sup> cells for 10× scRNA-seq. **b**, UMAP representation of CD45<sup>+</sup> Lymphoid (upper panel), CD45<sup>+</sup> Myeloid (middle panel) and CD45<sup>-</sup> (lower panel) cells showing replicate contribution,

batch effect correction and good sample mixing calculated with LISI (Korsunsky, Millard et al. 2019). **c**, Bar plots showing percentage of total cells divided into each cell type per replicate, CD45<sup>+</sup> Lymphoid (left panel), CD45<sup>+</sup> Myeloid (middle panel) and CD45<sup>-</sup> (right panel) cells.



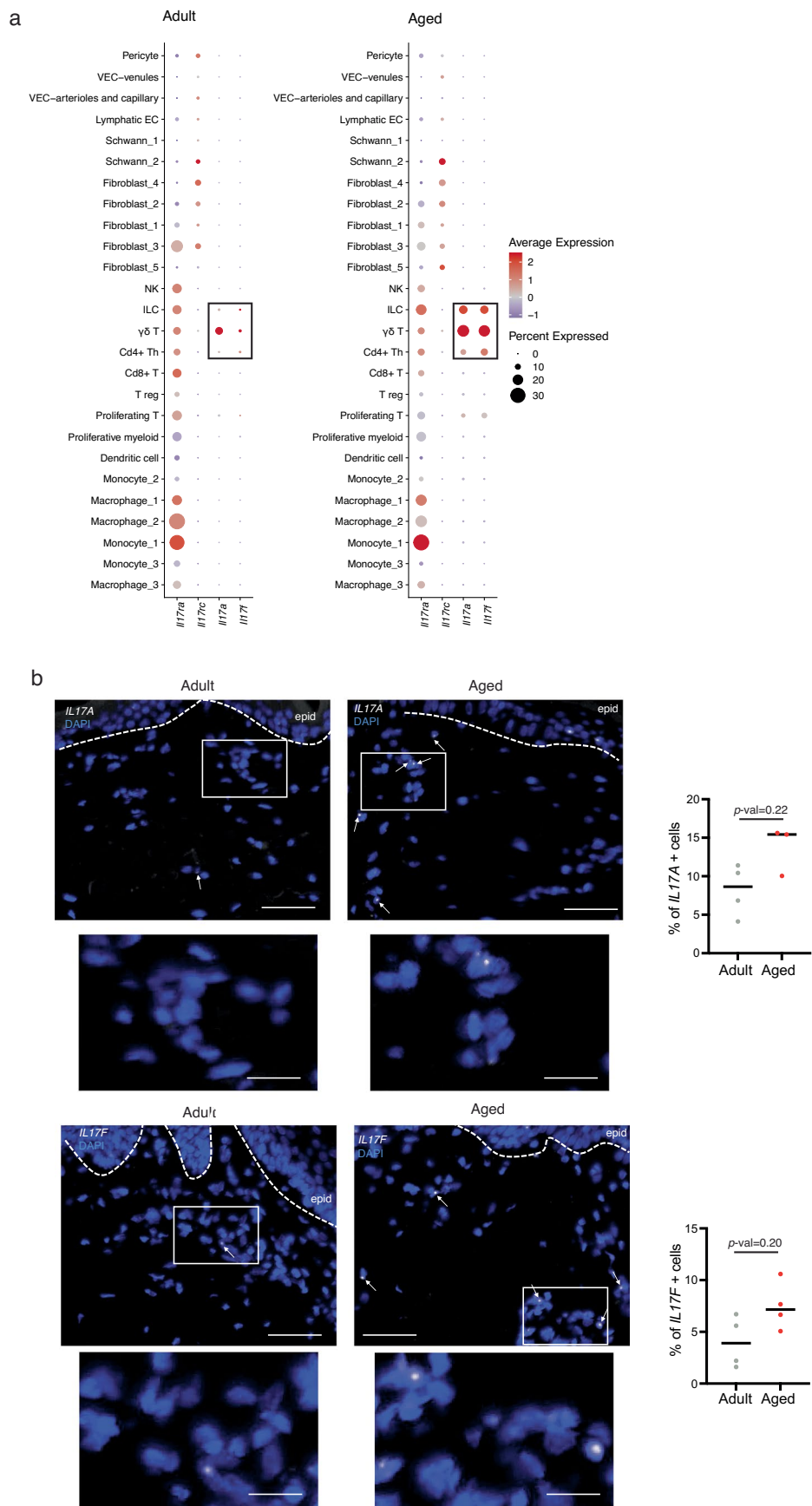
*scomp* (Mangiola 2022) obtained with the scRNA-seq data. Error bars indicate the 95% credible intervals, center line is the median. The black boxplots represent the observed data, while blue ones indicate the posterior predictive check of the model. Boxes colored in orange indicate statistically significant differences in cell proportion between conditions (FDR < 0.025 using Benjamini-Hochberg procedure to control for multiple testing).



Extended Data Fig. 3 | See next page for caption.

**Extended Data Fig. 3 | Changes observed in adult vs. aged dermis. a,b,** Box plots showing changes in proportion of (a) myeloid and (b) lymphoid cells in adult and aged conditions obtained with *sccomp* (Mangiola 2022) obtained with the scRNA-seq data. Error bars indicate the 95% credible intervals, center line is the median. The black boxplots represent the observed data, while blue ones indicate the posterior predictive check of the model. Boxes colored in orange indicate statistically significant differences in cell proportion between conditions (FDR < 0.025 using Benjamini-Hochberg procedure to control for multiple testing) and red triangles outside the boxes mark outliers. **c,** Plots of selected GO categories belonging to Biological Processes (BP) analysis for genes

upregulated in monocyte\_1 cluster (upper panel) and monocyte\_2 cluster (lower panel) upon aging. The x axis represents  $-(\log_{10})$  of the adjusted *P*-value for each depicted GO category. **d,** Violin plots showing expression levels of *Il1b* in cells belonging to clusters monocyte\_1, macrophage\_2, and dendritic cells in adult and aged conditions. **e,** Immunostaining for CD4 in adult (upper panel) and aged (lower panel) back skin. White arrows point to positive cells. Bar = 50  $\mu\text{m}$ . Insets are shown in the right panel next to each condition, bar = 10  $\mu\text{m}$ . \* = unspecific hair shaft autofluorescence. N = 5 individual mice. Quantification shows percentage of positive cells. Brightness and contrast were adjusted only for visualization purposes. Quantifications were done in raw images.

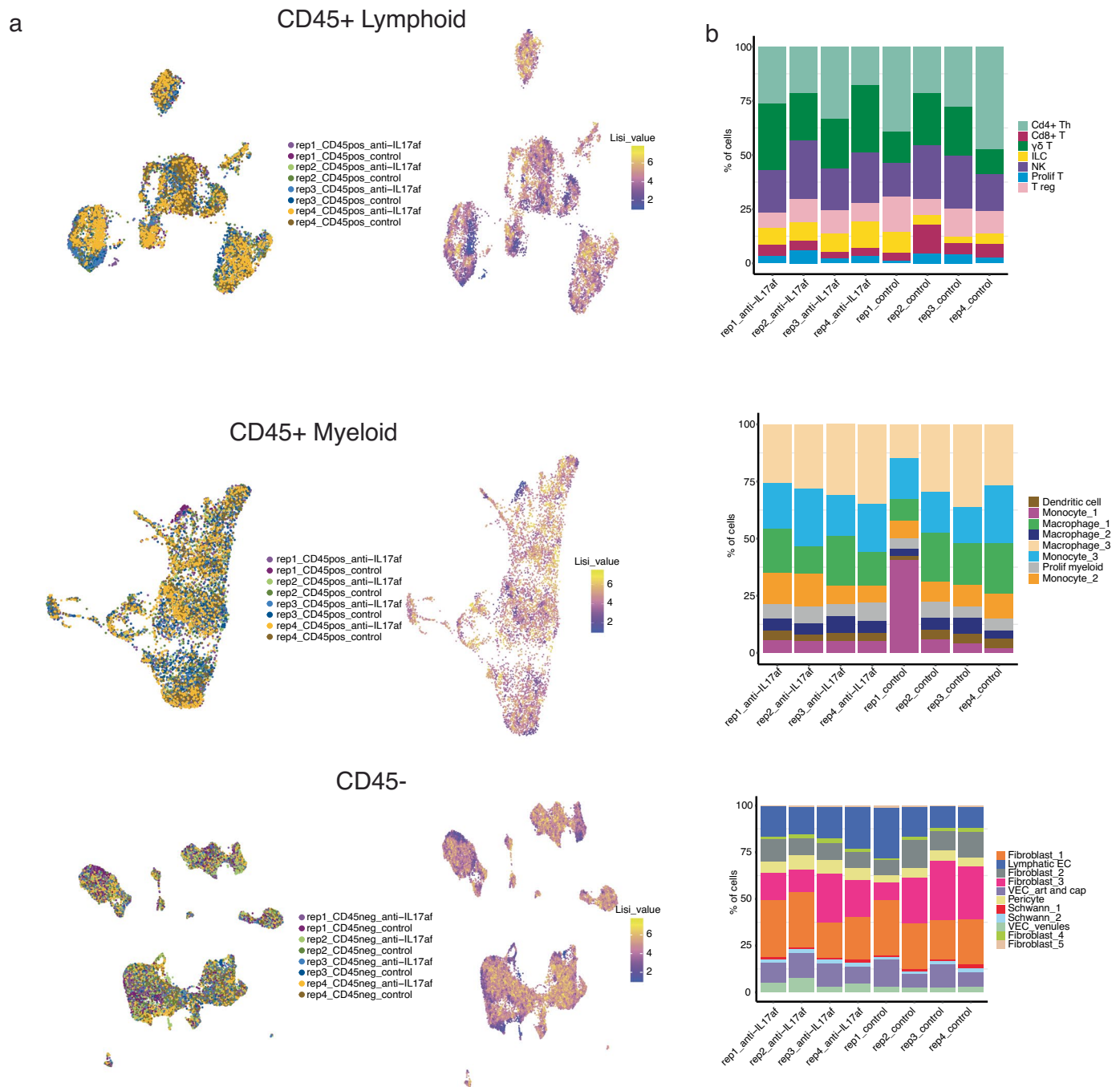


Extended Data Fig. 4 | See next page for caption.

**Extended Data Fig. 4 | IL-17 levels in adult and aged mouse and human skin.**  
**a.** Dot plot showing percentage of cells expressing and average expression of IL-17 receptors *Il17ra* and *Il17rc*, and ligands *Il17a* and *Il17f* in all dermal cell types. Black boxes enclose lymphoid subtypes that show differential expression of *Il17a* and *Il17f* upon aging. **b.** Fluorescent *in situ* hybridization (FISH) for *IL17A* (n = 4 individual donors for adult and n = 3 individual donors for aged) and

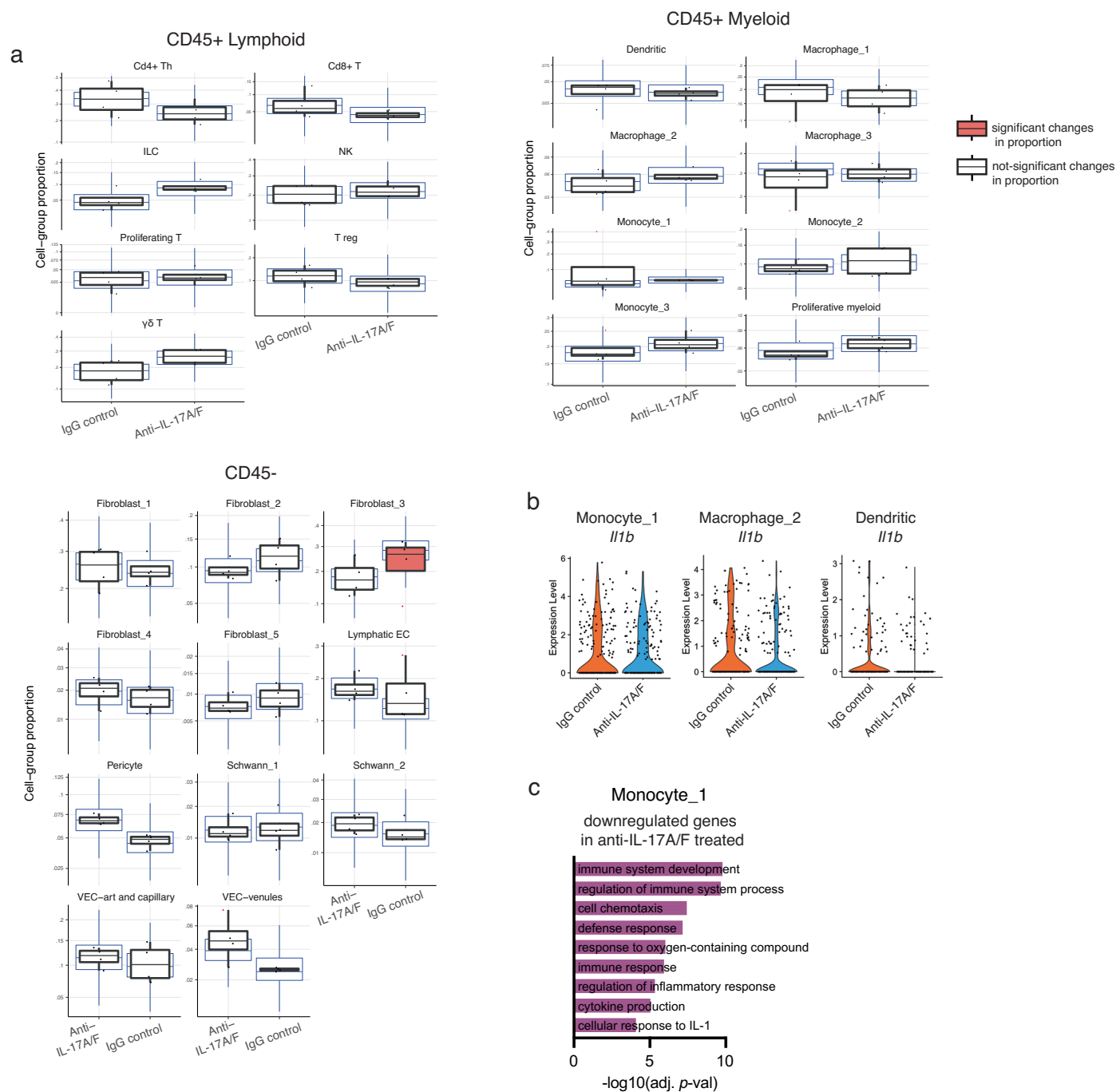
*IL17F* (n = 4 individual donors for each age) in adult and aged human skin (top panel). Bar = 50  $\mu$ m. White arrows point to positive cells. Insets with higher magnification focusing on the dermis in the bottom panel, bar = 10  $\mu$ m. Plot shows quantification in percentage of positive cells. Brightness and contrast were adjusted only for visualization purposes. Quantifications were done in raw images.





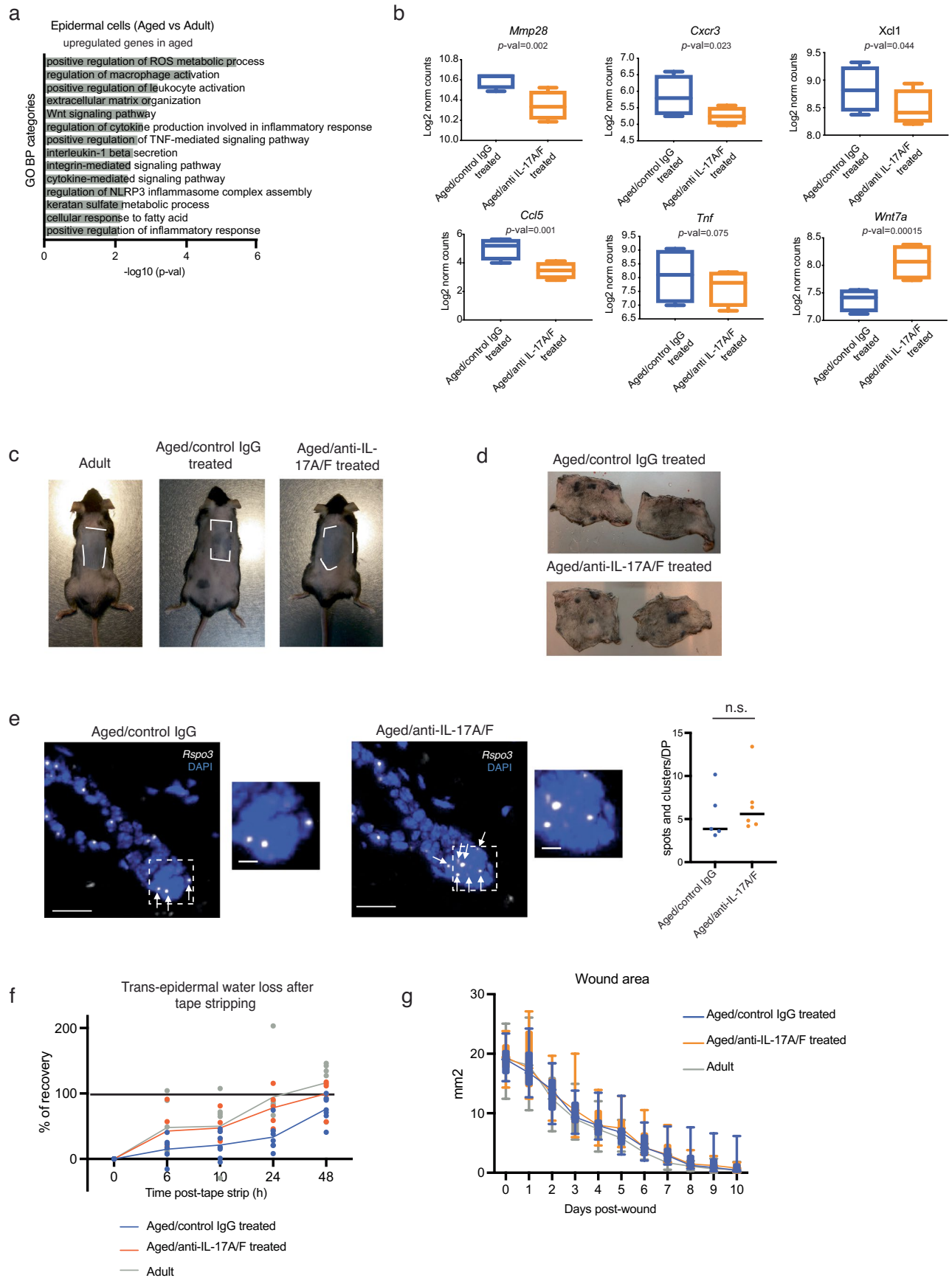
**Extended Data Fig. 5 | Quality controls of scRNA-seq of aged/control IG and aged/anti-IL-17 treated dermis. a,** UMAP representation of CD45+ Lymphoid (upper panel), CD45+ Myeloid (middle panel) and CD45- (lower panel) cells

showing replicate contribution and good sample mixing calculated with LISI. **b,** Bar plots showing percentage of each cell type per replicate in CD45+ Lymphoid (upper panel), CD45+ Myeloid (middle panel) and CD45- (lower panel) cells.



**Extended Data Fig. 6 | Changes observed by scRNA-seq in aged/control IgG and aged/anti-IL-17-treated dermis. a**, Box plots showing changes in proportion of CD45+ lymphoid (upper left panel), CD45+ myeloid (upper right panel), and non-immune CD45- (lower panel) cell populations calculated with *sccomp* (Mangiola 2022) obtained with the scRNA-seq data. Error bars indicate the 95% credible intervals, center line is the median. The black boxplots represent the observed data, while blue ones indicate the posterior predictive check of the model. Boxes colored orange indicate statistically significant differences

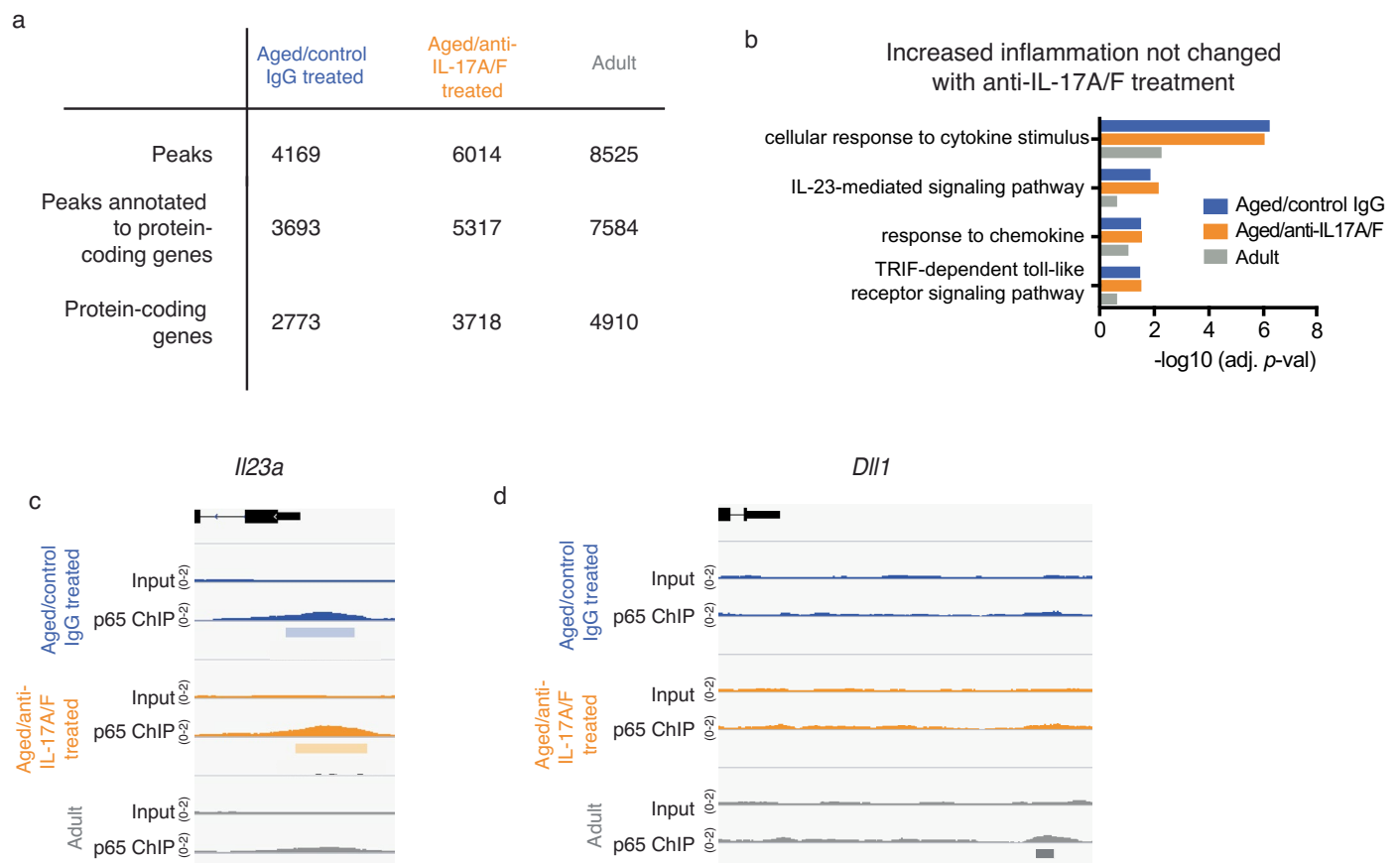
in cell proportion between conditions (FDR < 0.025 using Benjamini-Hochberg procedure to control for multiple testing) and red triangles mark outliers. **b**, Violin plots showing expression values of *Il1b* in cells belonging to clusters monocyte\_1, macrophage\_2, and dendritic cells after anti-IL-17A/F treatment. **c**, Plot of selected GO categories belonging to Biological Processes (BP) analysis for genes downregulated in monocyte\_1 upon IL-17A/F neutralization treatment. The x axis represents  $-(\log_{10})$  of the adjusted *P*-value for each depicted GO category.



Extended Data Fig. 7 | See next page for caption.

**Extended Data Fig. 7 | Readouts of anti-IL-17 treatment in aged mice. a,** Plot of selected GO categories belonging to BP analysis for genes upregulated upon aging in epidermal cells. The x axis represents  $-\log_{10}$  of the  $P$ -value for each depicted GO category. **b,** Box and whiskers plots (min to max, box Q1 to Q3, center depicts the median) showing expression levels of selected genes differentially expressed upon IL-17A/F blocking treatment in epidermal cells ( $n = 4$  individual mice per age). Depicted genes were extracted from the GO analysis shown in Fig. 4c. **c,** Images of adult, aged/IgG control and aged/anti-IL-17A/F antibody treated back skin showing the epilated areas (white dashed line areas). Note that the gray color of dermis indicates anagen progression. **d,** Representative images showing shaved mouse back skins with anagen patches (black areas) in aged/IgG control and aged/anti-IL-17A/F antibody treated. **e,** Representative images and quantification of *Rspo3* FISH in aged/IgG control

( $n = 5$  individual mice) and aged/anti-IL-17A/F antibody treated ( $n = 6$  individual mice) mouse back skin. Bar =  $20\mu\text{m}$ . White arrows point to positive cells. Insets are shown in the right panel next to each condition, bar =  $5\mu\text{m}$ . Plot shows the number of spots and clusters detected with *Rspo3* probe per dermal papilla. n.s., not significant. Brightness and contrast were adjusted only for visualization purposes. Quantifications were done in raw images. **f,** Plot showing percentage of recovery of trans-epidermal water loss (TEWL) after tape-stripping comparing i) adult, ii) aged/IgG control and iii) aged/anti-IL-17A/F antibody treated through time (0, 6, 10, 24, 48 hours post tape stripping). **g,** Box and whiskers plots (min to max, box Q1 to Q3) of wound area measurements (in  $\text{mm}^2$ ) through time comparing i) adult ( $n = 15$  individual mice), ii) aged/IgG control ( $n = 14$  individual mice) and iii) aged/anti-IL-17A/F antibody treated ( $n = 15$  individual mice). Average of the two wounds is used for this plot.



**Extended Data Fig. 8 | p65 ChIP in aged/control IgG and aged/anti-IL-17-treated epidermal cells. a**, Table summarizing the number of peaks, peaks annotated to protein-coding genes and unique protein-coding genes. Results obtained in a pooled sample containing 4 biological replicates per condition (adult, aged/IgG control and aged/anti-IL-17A/F antibody treated) of the p65 ChIP-seq. **b**, Plot comparing the adjusted *P*-values of selected GO categories of

genes bound by p65 in aged/IgG control, aged/anti-IL-17A/F antibody treated and adult epidermal cells. **c**, Snapshot of p65 binding to the regulatory area of *Il23a* gene in aged/IgG control, aged/anti-IL-17A/F antibody treated and adult epidermal cells. **d**, Snapshot of p65 binding upstream of the transcriptional start site of *Dll1* gene in aged/IgG control, aged/anti-IL-17A/F antibody treated and adult epidermal cells.

## Reporting Summary

Nature Portfolio wishes to improve the reproducibility of the work that we publish. This form provides structure for consistency and transparency in reporting. For further information on Nature Portfolio policies, see our [Editorial Policies](#) and the [Editorial Policy Checklist](#).

### Statistics

For all statistical analyses, confirm that the following items are present in the figure legend, table legend, main text, or Methods section.

n/a Confirmed

- The exact sample size ( $n$ ) for each experimental group/condition, given as a discrete number and unit of measurement
- A statement on whether measurements were taken from distinct samples or whether the same sample was measured repeatedly
- The statistical test(s) used AND whether they are one- or two-sided  
*Only common tests should be described solely by name; describe more complex techniques in the Methods section.*
- A description of all covariates tested
- A description of any assumptions or corrections, such as tests of normality and adjustment for multiple comparisons
- A full description of the statistical parameters including central tendency (e.g. means) or other basic estimates (e.g. regression coefficient) AND variation (e.g. standard deviation) or associated estimates of uncertainty (e.g. confidence intervals)
- For null hypothesis testing, the test statistic (e.g.  $F$ ,  $t$ ,  $r$ ) with confidence intervals, effect sizes, degrees of freedom and  $P$  value noted  
*Give  $P$  values as exact values whenever suitable.*
- For Bayesian analysis, information on the choice of priors and Markov chain Monte Carlo settings
- For hierarchical and complex designs, identification of the appropriate level for tests and full reporting of outcomes
- Estimates of effect sizes (e.g. Cohen's  $d$ , Pearson's  $r$ ), indicating how they were calculated

*Our web collection on [statistics for biologists](#) contains articles on many of the points above.*

### Software and code

Policy information about [availability of computer code](#)

**Data collection** A BD FACSAria Fusion flow cytometer was used to sort the cells for 10X single cell sequencing, using FACSDiva version 8.0.1. Hematoxylin and eosin (H&E) images, were acquired using a NanoZoomer scanner (Hamamatsu) at 20x magnification, in which 1 pixel corresponds to 0.46 $\mu$ m, and coupled to a mercury lamp unit L11600-05 and using NDP.scan 3.4 software U10074-03 (Hamamatsu, Photonics, France).

**Data analysis** For flow cytometry analyses, FlowJo v10.0.8.r1 was used. Scaled images were analyzed with Qupath (v0.3.0 and v0.3.2). All graphical representations were performed with GraphPad Prism 9. For the RNA Sequencing data, STAR 2.5.2b, R 3.5.1, DESeq2 1.22.1, and R Subread package v1.32.4 were used. For the 10X single cell sequencing data, Cell Ranger pipeline v6.0.0 and the Seurat package v4.0.4 in R v4.0.3, were used. Local inverse Simpson's Index (LISI) was used to ensure good sample integration. To check significance of differences in cell composition of samples, sccomp was used.

For manuscripts utilizing custom algorithms or software that are central to the research but not yet described in published literature, software must be made available to editors and reviewers. We strongly encourage code deposition in a community repository (e.g. GitHub). See the Nature Portfolio [guidelines for submitting code & software](#) for further information.

## Data

Policy information about [availability of data](#)

All manuscripts must include a [data availability statement](#). This statement should provide the following information, where applicable:

- Accession codes, unique identifiers, or web links for publicly available datasets
- A description of any restrictions on data availability
- For clinical datasets or third party data, please ensure that the statement adheres to our [policy](#)

The 10X single cell and RNA sequencing datasets generated during and/or analysed during the current study are available in the GEO repository, <https://www.ncbi.nlm.nih.gov/geo/query/acc.cgi?acc=GSE190182>; <https://www.ncbi.nlm.nih.gov/geo/query/acc.cgi?acc=GSE190393>; <https://www.ncbi.nlm.nih.gov/geo/query/acc.cgi?acc=GSE193920>; <https://www.ncbi.nlm.nih.gov/geo/query/acc.cgi?acc=GSE213732>. ScRNA-seq analysis scripts are in <https://github.com/mereulab/IL17-SkinAging>. Gene ontology biological processes software can be found in g:Profiler86 (<https://biit.cs.ut.ee/gprofiler/gost>). The rest of the data generated or analyzed during this study are included in this published article (and its supplementary information files).

## Human research participants

Policy information about [studies involving human research participants and Sex and Gender in Research](#).

Reporting on sex and gender	For this study, healthy skin from 2 adult men, 2 adult women, 2 aged men and 2 aged women. These samples were commercially available at Genoskin (France).
Population characteristics	Adults were aged 22 to 29 and aged individuals were from 60 to 72 years old. All skin samples were from healthy volunteer donors.
Recruitment	Samples were purchased from Genoskin (France), and were selected from their catalogue to match our sex and age choice.
Ethics oversight	French Ethics Committee (Comité de Protection de Personnes or CPP) and the French Ministry of Research and Higher Education

Note that full information on the approval of the study protocol must also be provided in the manuscript.

## Field-specific reporting

Please select the one below that is the best fit for your research. If you are not sure, read the appropriate sections before making your selection.

- Life sciences       Behavioural & social sciences       Ecological, evolutionary & environmental sciences

For a reference copy of the document with all sections, see [nature.com/documents/nr-reporting-summary-flat.pdf](https://www.nature.com/documents/nr-reporting-summary-flat.pdf)

## Life sciences study design

All studies must disclose on these points even when the disclosure is negative.

Sample size	No statistical methods were used to pre-determine sample sizes. This was decided taking into the account the variability existing between samples, particularly in aged mice, and was based on previous experience of the authors with aged mice, especially in skin. Sample size is included in the figure legends for each experiment and/or in the methods section.
Data exclusions	Mice with skin wounds (fighting or dermatitis) were excluded due to possible interference with the data. For experiments that required enzymatic digestion, female mice were used due to differences in skin digesting efficiency between sexes, as longer male skin digestion times are required and this reduced the survival of sorted dermal cells, skewing the results towards the most resilient cell types. For the rest of experiments, balances numbers between males and females were used.
Replication	All biological replicates for each experiment are included in the figure legends and the methods section. The majority of experiments included at least three or more biological and technical replicates, except for some of the 10x single cell sequencing data, which was obtained in duplicates. We obtained similar results in all different replicates, and key results were further confirmed with additional experimental approaches.
Randomization	For the IL-17 blocking experiments, mice were randomized and changed into cages different from the ones in which they were housed prior to the experiment. Randomization was not conducted for the rest of the experiments carried out, as these were performed on already randomized animals in each condition. Animals used for the same experiments were obtained from different cages, in order to avoid generating bias.
Blinding	Blinding was not carried out in the majority of the experiments as the same investigators processed all the experiments and analysed the data. For the histopathological assessments and quantifications, the investigator analyzing the data was blinded as to the condition being quantified.

# Reporting for specific materials, systems and methods

We require information from authors about some types of materials, experimental systems and methods used in many studies. Here, indicate whether each material, system or method listed is relevant to your study. If you are not sure if a list item applies to your research, read the appropriate section before selecting a response.

## Materials & experimental systems

n/a	Involved in the study
<input type="checkbox"/>	<input checked="" type="checkbox"/> Antibodies
<input checked="" type="checkbox"/>	<input type="checkbox"/> Eukaryotic cell lines
<input checked="" type="checkbox"/>	<input type="checkbox"/> Palaeontology and archaeology
<input type="checkbox"/>	<input checked="" type="checkbox"/> Animals and other organisms
<input checked="" type="checkbox"/>	<input type="checkbox"/> Clinical data
<input checked="" type="checkbox"/>	<input type="checkbox"/> Dual use research of concern

## Methods

n/a	Involved in the study
<input type="checkbox"/>	<input checked="" type="checkbox"/> ChIP-seq
<input type="checkbox"/>	<input checked="" type="checkbox"/> Flow cytometry
<input checked="" type="checkbox"/>	<input type="checkbox"/> MRI-based neuroimaging

## Antibodies

Antibodies used	anti-IL-17A (clone 17F3, #BE0173 BioXCell), anti-IL-17F (clone MM17F8F5.1A9, #BE0303 BioXCell), IgG1 (clone MOPC-2, #BE0083 BioXCell), CD45-APC (clone 30-F11, 1:100, #559864 BD Biosciences), EpCAM-PE (clone G8.8, 1:200, #552370 BD Biosciences), IL-17A (rabbit polyclonal, 1:200, ab79056 Abcam), CD4 (clone 4SM95, rat, 1:100, #14-9766-82 ThermoFisher), C anti-Rabbit Alexa Fluor 488 (donkey polyclonal, 1:400, #A-21206 Molecular Probes), anti-Rat Alexa Fluor 647 (goat polyclonal, 1:500, #A-21247 ThermoFisher) and p65 (4ug/ml, #8242 Cell Signalling Technology).
Validation	All antibodies were purchased after prior literature research, and all usage was carried out according to datasheet instructions or previously published protocols analyzing similar parameters. For IL-17A immunostaining, the antibody was used on IL-17 KO murine skin in order to validate its specificity. This antibody reacts with human and murine sample, as described by abcam. In the case of in vivo injections, antibody validation was carried out by comparing the data obtained to an irrelevant IgG1 control. IL-17A, IL-17F and IgG antibodies used for injections have been approved for murine usage by BioXCell. No further validation was carried out.

## Animals and other research organisms

Policy information about [studies involving animals](#); [ARRIVE guidelines](#) recommended for reporting animal research, and [Sex and Gender in Research](#)

Laboratory animals	Retired C57Bl/6J breeder females were purchased from Charles River and were aged until the desired age in the animal facility at the Barcelona Science Park (PCB). In some cases, when smaller cohorts were needed, aged mice were bred in-house to obtain sex-balanced groups. Control adult mice were either bred in-house or purchased to Charles River to generate matching cohorts. Aged mice were between 80- to 90-weeks of age, and adult mice were between 17-to 25-weeks of age. The temperature of the animal facility was kept between 20 to 24°C, and the humidity ranged from 45% to 65%.
Wild animals	The study did not involve wild animals.
Reporting on sex	Mostly female mice were used due to the purchasing of aging retired breeders, and to differences between skin digesting efficiency between sexes, as longer male skin digestion times are required and this reduced the survival of sorted dermal cells, skewing the results towards the most resilient cell types. For the other type of samples not involving enzymatic digestion, both sexes were used.
Field-collected samples	The study did not involve field-collected samples
Ethics oversight	All procedures were evaluated and approved by the Ethical Committee for Animal Experimentation (CEEA) from the Government of Catalunya.

Note that full information on the approval of the study protocol must also be provided in the manuscript.

## ChIP-seq

### Data deposition

- Confirm that both raw and final processed data have been deposited in a public database such as [GEO](#).
- Confirm that you have deposited or provided access to graph files (e.g. BED files) for the called peaks.

Data access links

*May remain private before publication.*

Files in database submission



Files in database submission	GSE213732_featureCounts_mm10.xlsx (count matrix) GSE213732_RAW.tar (bed files)
Genome browser session (e.g. <a href="#">UCSC</a> )	no longer applicable

## Methodology

Replicates	4 replicates (1 individual mouse per replicate was used) per condition (adult, aged/IgG control treated, aged/anti-IL-17 treated)
Sequencing depth	All reads were 50bp, single-end. Adult input R1 35789169 aged/IgGcontrol input R1 35314617 aged/anti-IL-17 input R1 36601359 Adult input R2 35341249 aged/IgGcontrol input R2 34109883 aged/anti-IL-17 input R2 37512657 Adult input R3 35642578 aged/IgGcontrol input R3 34839385 aged/anti-IL-17 input R3 40916830 Adult input R4 39819971 aged/IgGcontrol input R4 38430481 aged/anti-IL-17 input R4 38610390 Adult ChIP R1 37511829 aged/IgGcontrol ChIP R1 39082862 aged/anti-IL-17 ChIP R1 35144765 Adult ChIP R2 38773737 aged/IgGcontrol ChIP R2 33945273 aged/anti-IL-17 ChIP R2 40762556 Adult ChIP R3 34345069 aged/IgGcontrol ChIP R3 32243427 aged/anti-IL-17 ChIP R3 34629334 Adult ChIP R4 34478668 aged/IgGcontrol ChIP R4 36927691 aged/anti-IL-17 ChIP R4 33583864
Antibodies	p65; Cell Signaling Technology ref 8242
Peak calling parameters	Peaks were called in these pooled files with MACS2 with -q 0.01 --nomodel --extsize 300 -B --SPMR parameters; mm10 genome reference was used
Data quality	Reads were trimmed and low quality reads were dropped from the analysis.
Software	Trimmomatic (version 0.36), Burrows-Wheeler aligner (version 0.7.12), SAMtools (version 1.5), MACS2, Homer (version 4.11)

## Flow Cytometry

### Plots

Confirm that:

- The axis labels state the marker and fluorochrome used (e.g. CD4-FITC).
- The axis scales are clearly visible. Include numbers along axes only for bottom left plot of group (a 'group' is an analysis of identical markers).
- All plots are contour plots with outliers or pseudocolor plots.
- A numerical value for number of cells or percentage (with statistics) is provided.

### Methodology

Sample preparation	In all cases, skins were floated (dermis-side down) in a Dispase II solution (5 mg/mL) in PBS for 30- to 40 min at 37°C. Epidermises were removed with a scalpel. For dermal cell isolation dermises were mechanically dissociated and then further digested in Liberase TM (6.5 Wünsch units/reaction) in DMEM (41965) for 20 to 30 min at 37°C with gentle agitation. Afterwards, DNase I (1 mg/ml) was added to the mix and incubated for 15 min at 37°C without agitation. Digested dermises were strained first through a 100-µm strainer and then through a 40-µm strainer to obtain single-cell suspensions. For epidermal cell isolation epidermises were removed with a scalpel and mechanically dissociated. They were then strained through a 100-µm and then a 40-µm strainer to obtain single-cell suspensions  For 10X scRNA-seq, single-cell dermal suspensions were incubated with CD45-APC and EpCAM-PE for 45 min on ice. After two washes in PBS, cells were resuspended in 2 µg/ml DAPI to stain DNA.
--------------------	---

Instrument	BD FACSAria Fusion flow cytometer
Software	Flow cytometry data was collected using BD FACSDiva software v8.0.1 and analyzed using FlowJo v10.0.8.r1.
Cell population abundance	For CD45+ cells, around 17% of the stained dermal population was analyzed, and CD45- cells, around 90% of that same population. These percentages were dependent on the sample analyzed.
Gating strategy	In all cases, forward scatter (FSC) vs side scatter (SSC) plot was generated to separate cells from cellular debris. Then, doublets were excluded from single cells by plotting FSC-area vs FSC-width. To eliminate dead cells, FSC-area was plotted against DAPI (VIO F) channel and cells that were positive for DAPI were excluded. For 10X scRNA-seq CD45+/- cells were obtained and EpCAM+ cells excluded. In all cases, the gatings were set according to the corresponding FMO and single controls. An example of the sorted cells obtained is provided in Supplementary Figure 1.

Tick this box to confirm that a figure exemplifying the gating strategy is provided in the Supplementary Information.